CHAPTER – 5

AA 6082 Al-alloy based Metal Matrix Composite Reinforced with Non-equiatomic AlSiCrMnFeNiCu HEA

CHAPTER 5

AA 6082 Al-alloy based Metal Matrix Composite Reinforced with Non-equiatomic AlSiCrMnFeNiCu HEA

Al-based metal matrix composites (AMCs) have always attracted the attention of researcher and the industries due to their enhanced physical and mechanical properties [212]. The properties of the AMCs can be tailored by reinforcing them with suitable reinforcement and can be improved. These AMCs have better properties than Al and its alloys. Among the Al alloys, the age-hardenable AA 6082 Al offers the right combination of strength, extrudability, and corrosion resistance [216]. The AMCs, usually reinforced with conventional reinforcement like SiC, Al_2O_3, nitrides, etc., possess additional challenges about recycling, and machining [294,385]. However, the AMCs reinforced with suitable intermetallics offer good interfacial stability, better room temperature, and high-temperature strength [246]. In the past two decades, multicomponent high-entropy alloys (HEAs) having five or more principal elements either in the equiatomic, near equiatomic, or non–equiatomic ratio have been developed , which illustrated high hardness, excellent and high-temperature strength, and better corrosion resistance [192]. These HEAs properties have been exploited in recent years, as a suitable reinforcement for AMCs [270,277,337,339,340,403]. These AMCs reinforced with HEAs have shown promising results due to interfacial strengthening during processing, fabrication and heat treatment [270,277,337,339,340,403].

In the present work, efforts were made to study the structural, morphological, and phase composition of non–equiatomic $Al_{40}(SiCrMnFeNiCu)_{10}$ (at%) HEA and as a reinforcement in AA 6082 Al matrix. This composite material synthesized through vacuum induction melting and mechanical milling (MM) will be indicated as Al-HEA composite. The structural, morphological, microstructure and chemical composition were characterized through XRD, TEM and SEM techniques. The thermal stability of these Al-

HEA nanocomposite powder was studied through differential scanning calorimetry (DSC). Efforts were made to co-relate heating events of DSC with the phases evolved during in-situ XRD. Further, the Al-HEA bulk composite was fabricated through pressureless sintering for studying the transitional layer formation arising out from the interfacial reaction. The microstructural features and microhardness of Al–HEA composites were investigated through SEM and instrumented indentation technique. The Al–HEA composite fabricated by pressureless sintering has exibhited appreciable increase in hardness due to the homogenous distribution of reinforcement and the transitional layer formation at the interface.

5.1 Phase analysis of non–equiatomic AlSiCrMnFeNiCu HEA

The as-cast non–equiatomic HEA has a density of 5.08 $g.cm^{-3}$ and has a high hardness of 7.5 GPa. The detailed phase analysis of the as-cast and milled powder was done through XRD and TEM in the following sections.

5.1.1 XRD analysis of HEA

Figure 5.1 (a) and (b) shows the phase evolved in the as-cast and vibratory milled non–equiatomic $Al_{40}(SiCrMnFeNiCu)_{10}$ (at%) HEA respectively. The non-equiatomic HEA prepared by milling of as-cast samples will be referred to as HEA for the sake of simplicity. It is clear from Figure 5.1 (a) that the as-cast HEA contains two types of phases, i.e., a major phase corresponding to the B2-type and a minor phase corresponding to the Cr_5Si_3. The major phase have all the reflections (i.e., (100), (110), (111), (200), (210), (211)) corresponding to the B2-type (AlFe) phase (PDF card no.: 65-3201; a=0.29 nm; cP2; $Pm\bar{3}m$).

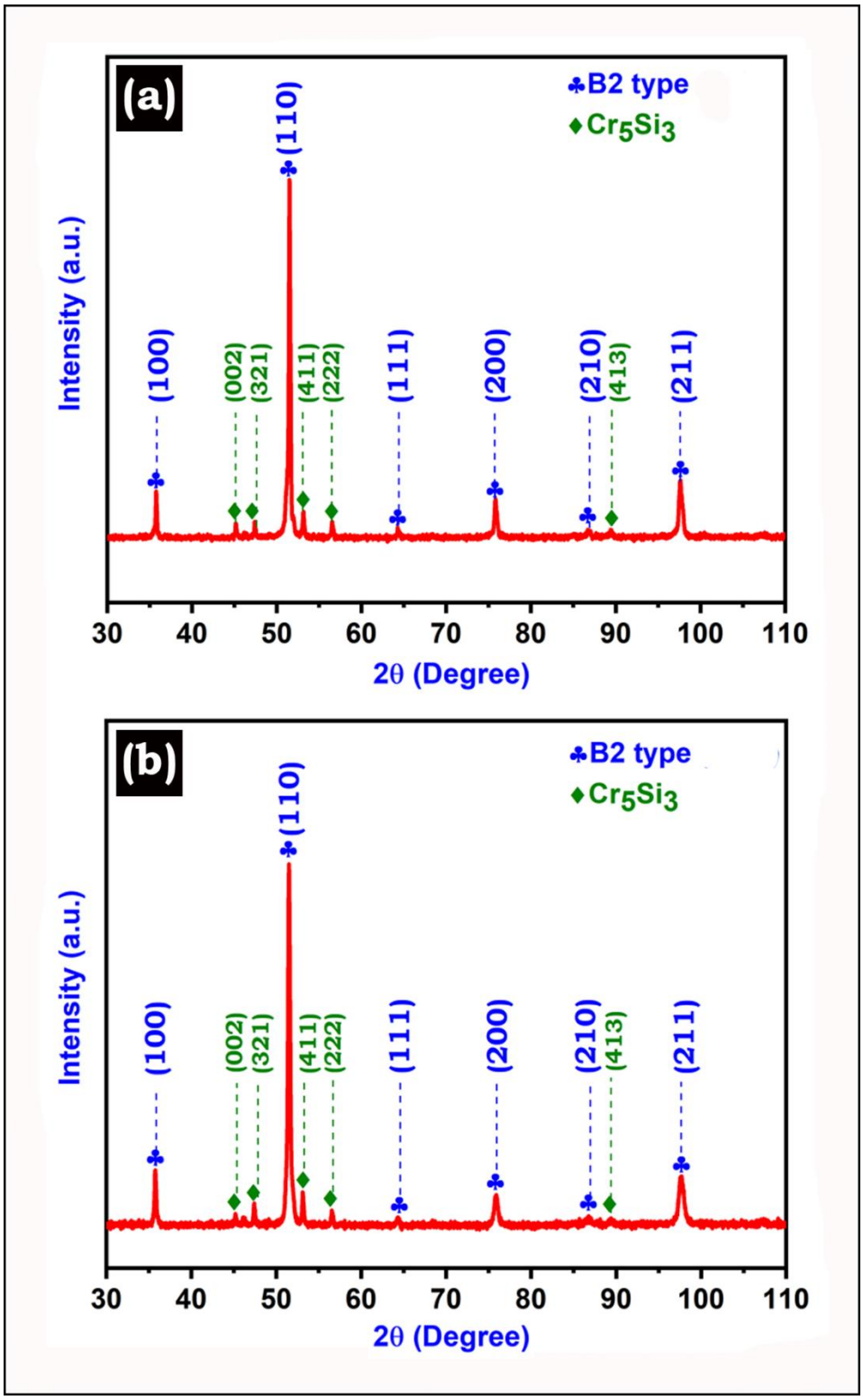

Figure 5. 1: XRD pattern of (a) as-cast and (b) powdered non-equiatomic HEA.

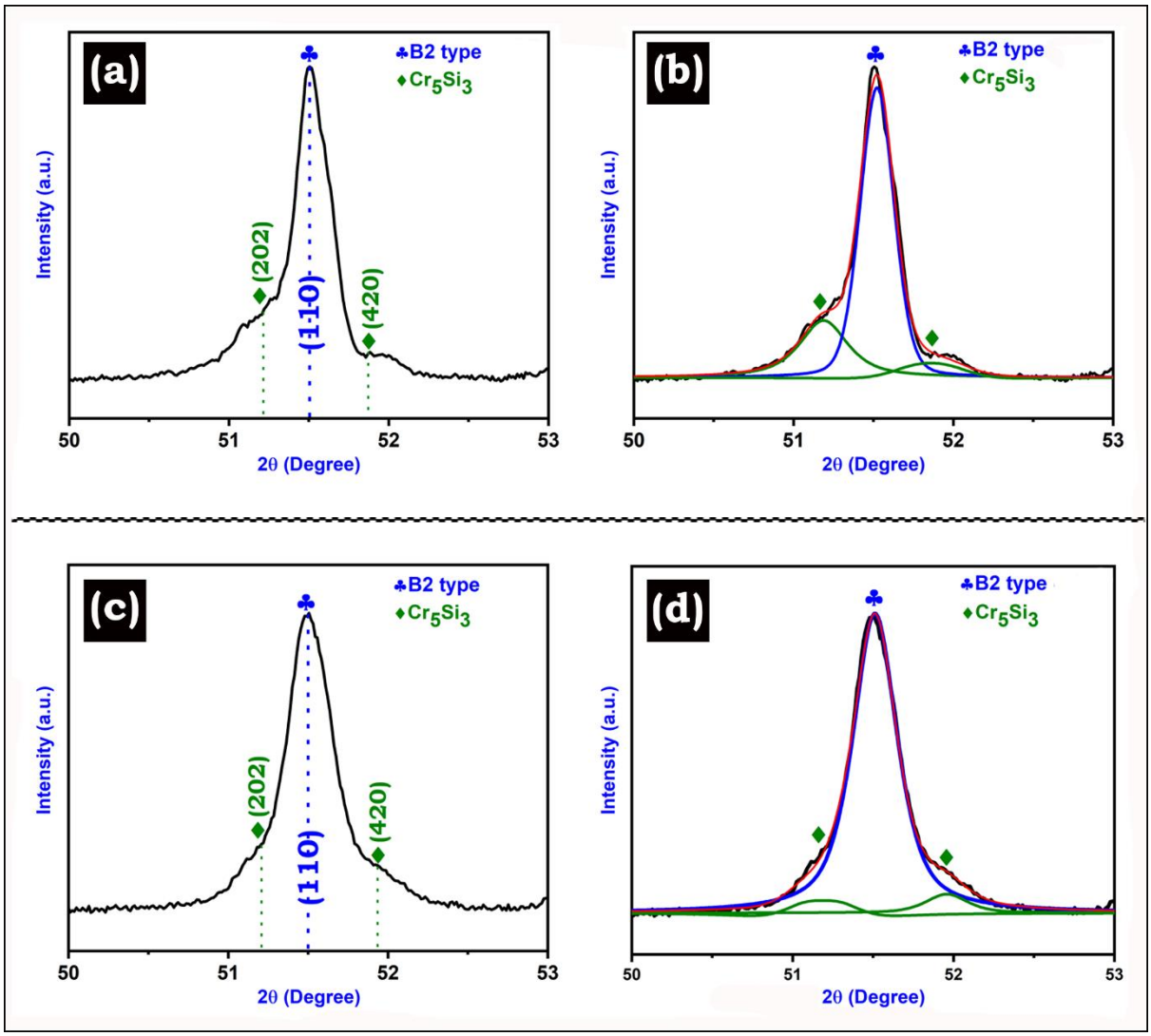

Figure 5. 2: Enlarged and de-convoluted XRD pattern showing the co-existence of B2-type phase and C_5Si_3 phase in (a, b) as-cast HEA and (c, d) powdered HEA, respectively.

It will be challenging to assess the major phase evolved after melting of the HEA belong to either the B2-AlFe type or AlNi type phase. However, this phase will be referred to as the B2-type Phase. The minor phase have all intense reflection (002) (d~0.231 nm), (321) (d~0.222 nm), (411) (d~0.2004 nm), (222) (d~0.1885 nm), (413) (d~0.126 nm) corresponding to the teragonal Cr_5Si_3 (PDF card no.: 00-051-1357; a=0.9165 nm, c=0.4638 nm; tI32; I4/mcm). The B2-type phase and a minor Cr_5Si_3 phase was observed in the as-cast HEA powdered through milling (Figure 5.1 (b)). The phase fraction of the major and

minor phases in the as-cast HEA was calculated and found to be ~95.6% and 4.4%, respectively. The as-cast HEA milled 30 min does not impart structural changes in the phases formed after melting of the HEA. Further, the ordering in powdered HEA was retained even after 30 min of milling with a ball to powder ratio (BPR) 100:1, as evident from the (100) reflection of the B2-type phase.

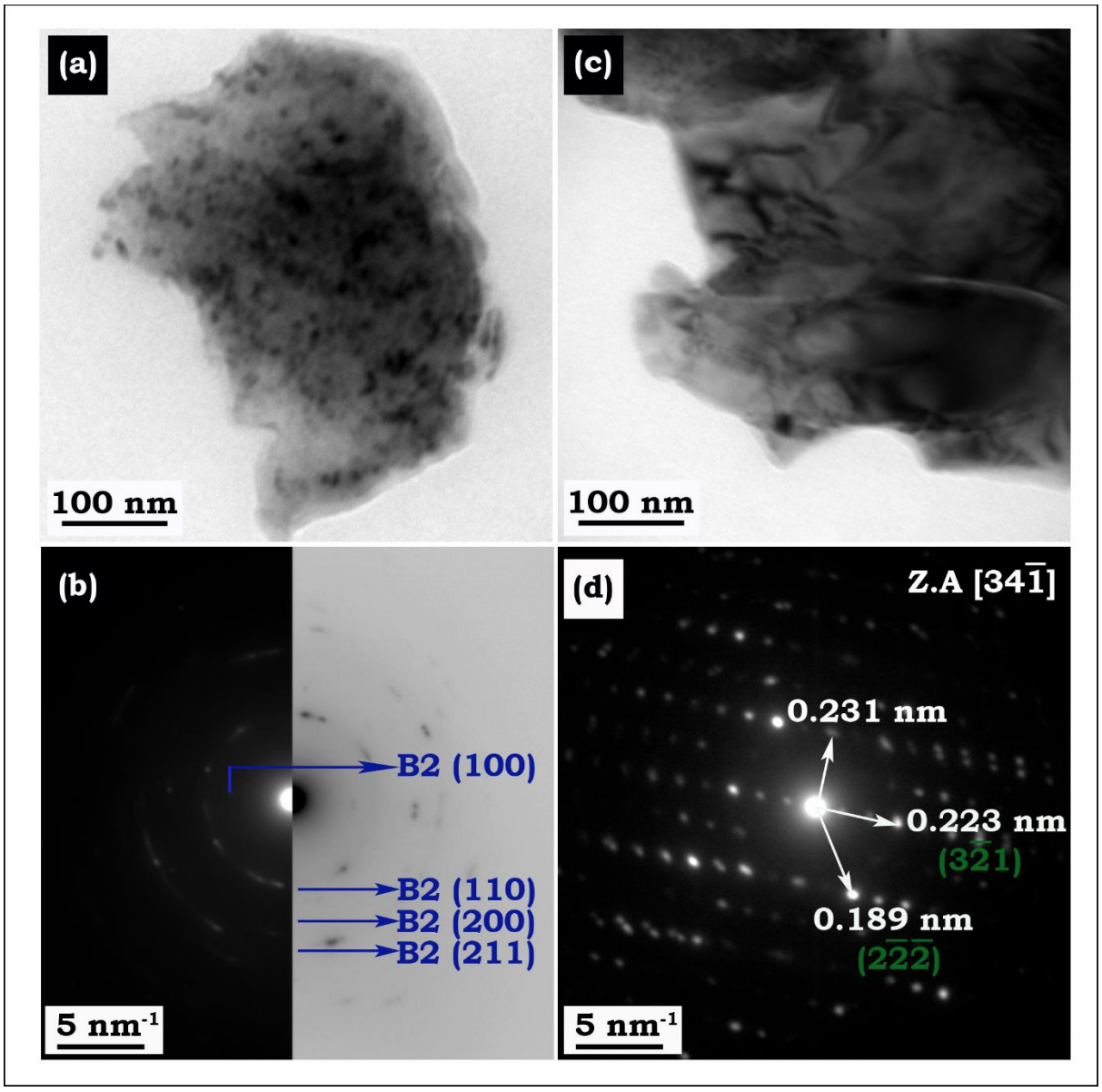

Figure 5. 3: (a) Bright-field image and (b) selected area diffraction (SAD) pattern showing the powder particle corresponding to B2-type phase respectively; (c) Bright-field image and (d) SAD pattern showing the powder particle corresponding to Cr_5Si_3 phase respectively.

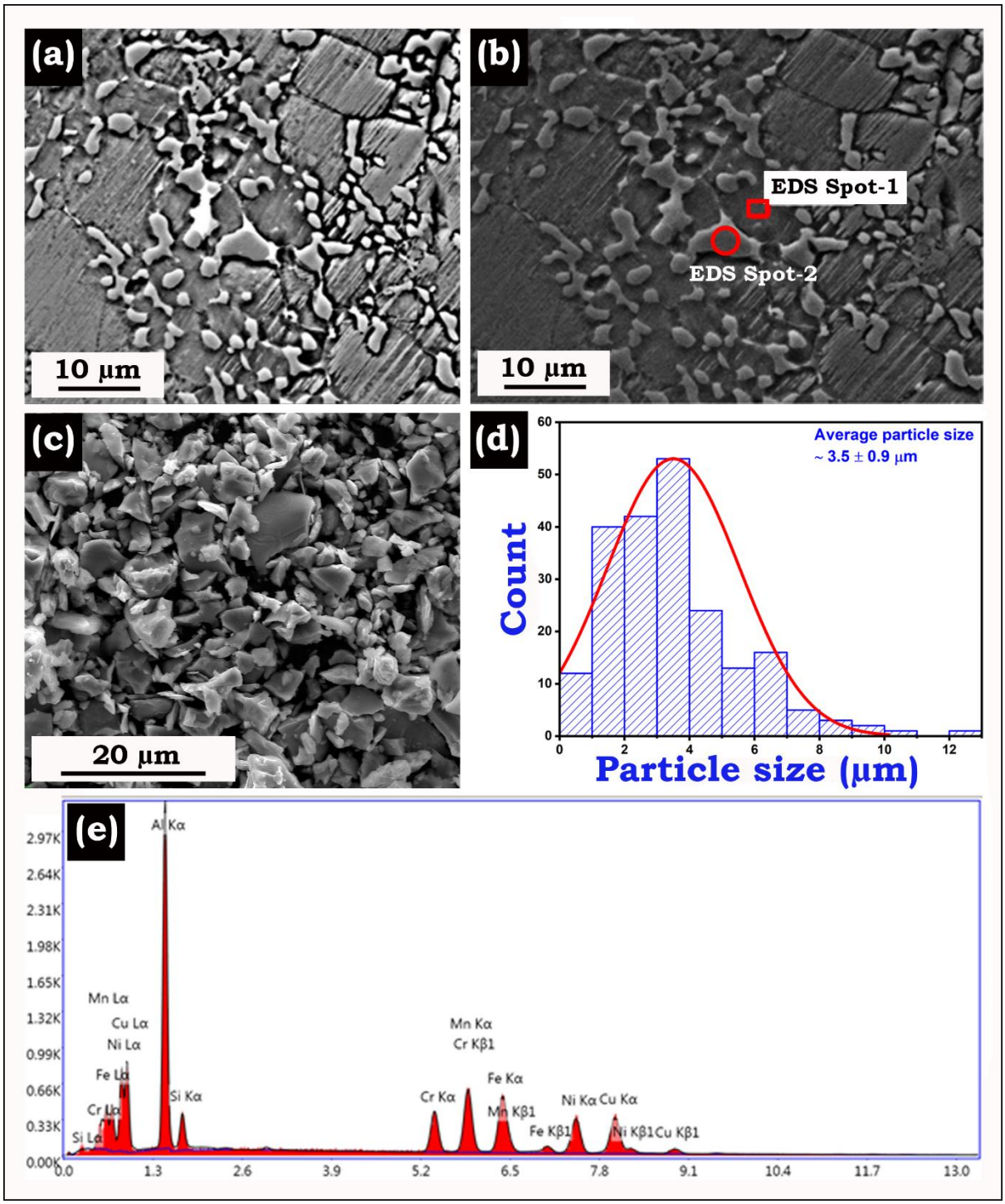

Figure 5. 4: (a) SEM micrograph of as-cast HEA sample, (b) SEM micrograph showing the region of EDS point analysis. (c) SEM micrograph showing the morphology of fragmented as-cast powdered HEA sample, (d) Particle size distribution of fragmented powder HEA particles; (e) EDS spectrum of as-cast HEA.

The existence of a major B2-type phase and a minor Cr_5Si_3 phase can be discerned through the enlarged and de-convoluted XRD pattern shown in Figure 5.2. The enlarged XRD pattern (Figure 5.2 (a)) in the 2θ range of 50º - 53º shows the presence of a B2-type phase corresponding (110) reflection having d-spacing ~0.2056 nm in the as-cast HEA sample. The minor Cr_5Si_3 phase was also evident from the (202) and (420) reflection having d-spacing ~0.2069 nm and 0.2047 nm, respectively. These peaks correspond to the two most intense reflection of the minor Cr_5Si_3 phase.

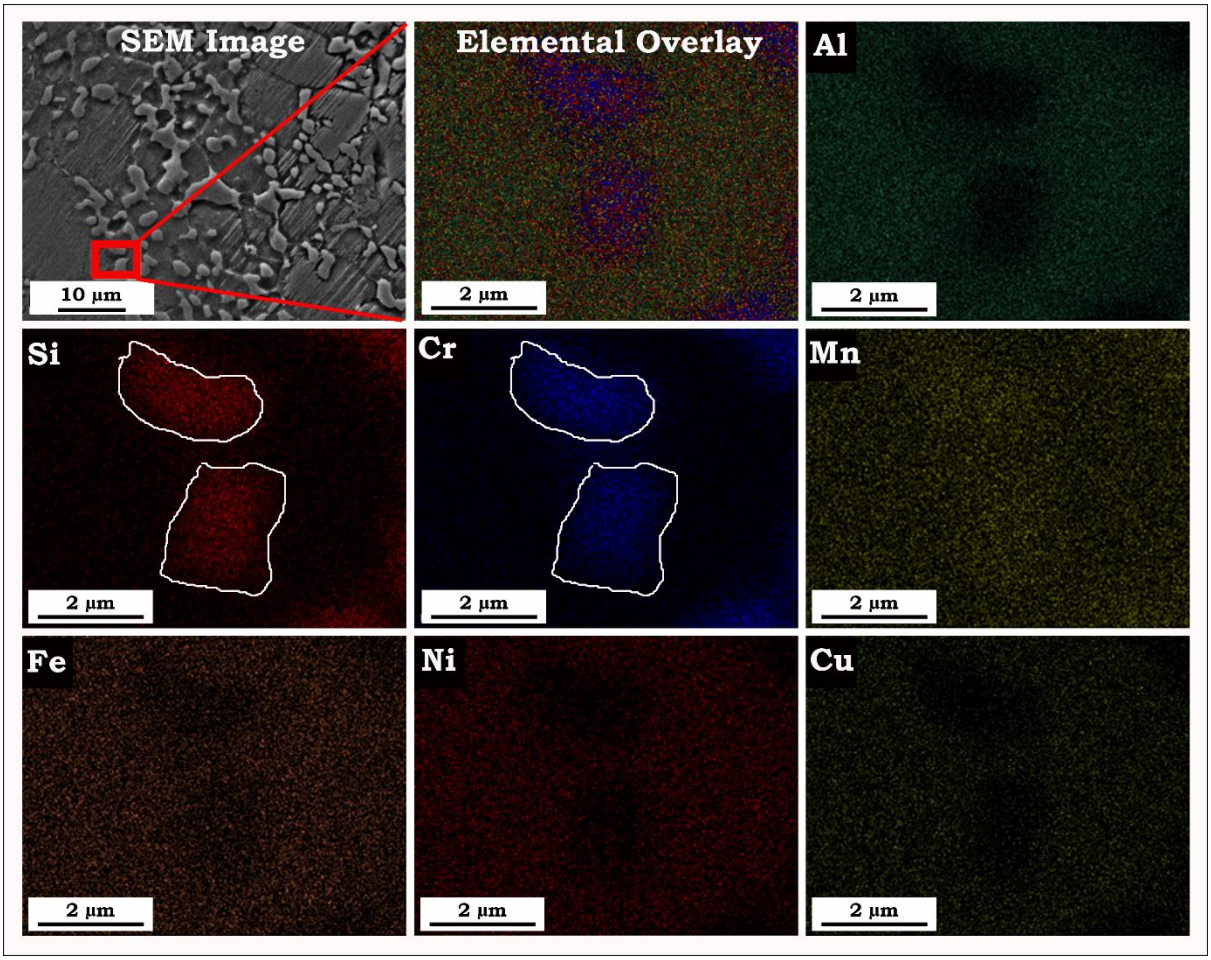

Figure 5. 5: SEM-EDS elemental mapping showing the distribution of alloying elements along with the presence of Cr, Si-rich region in as-cast HEA.

The asymmetric peaks in the 2θ range of 50° to 53° along the (110) reflection of the B2-type phase were de-convoluted to establish the minor phases presence. The de-

convoluted peak shown in Figure 5.2 (b) illustrates the major B2-type and minor Cr_5Si_3 phase. The goodness of the fit for all the three peaks were more than 95%. A similar observation was made for powdered HEA sample, as shown in Figure 5.2 (c & d). It can be discerned from the de-convoluted peak corresponding to the minor Cr_5Si_3 phase shown in Figure 5.2 (d) that the phase fraction of the minor phase decreases compared to the as-cast HEA. This can be correlated with the XRD pattern shown in Figure 5.1 (a) and (b), where it can be clearly seen that the asymmetricity associated with the (110) reflection of the B2-type phase corresponding to the minor phase decreases after 30 min of milling of the as-cast HEA sample.

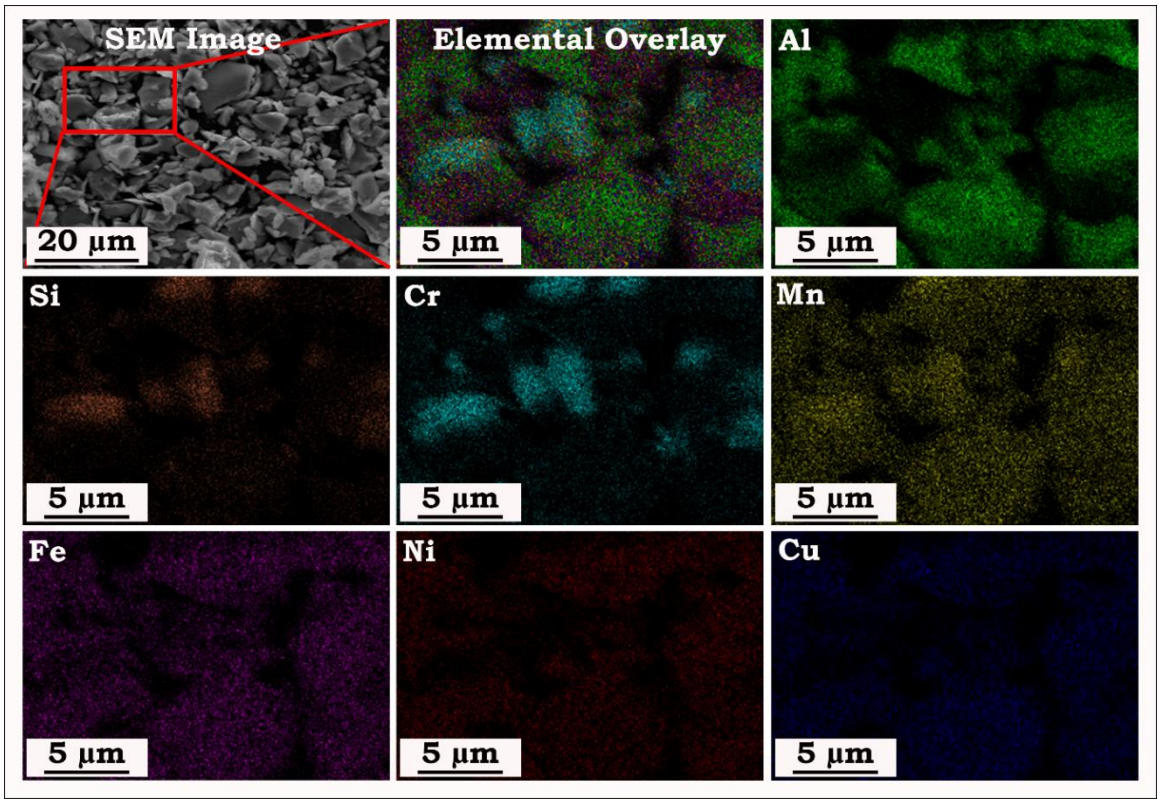

Figure 5. 6: SEM-EDS elemental mapping showing the distribution of alloying elements along with the presence of Cr, Si-rich region in as-cast powdered HEA.

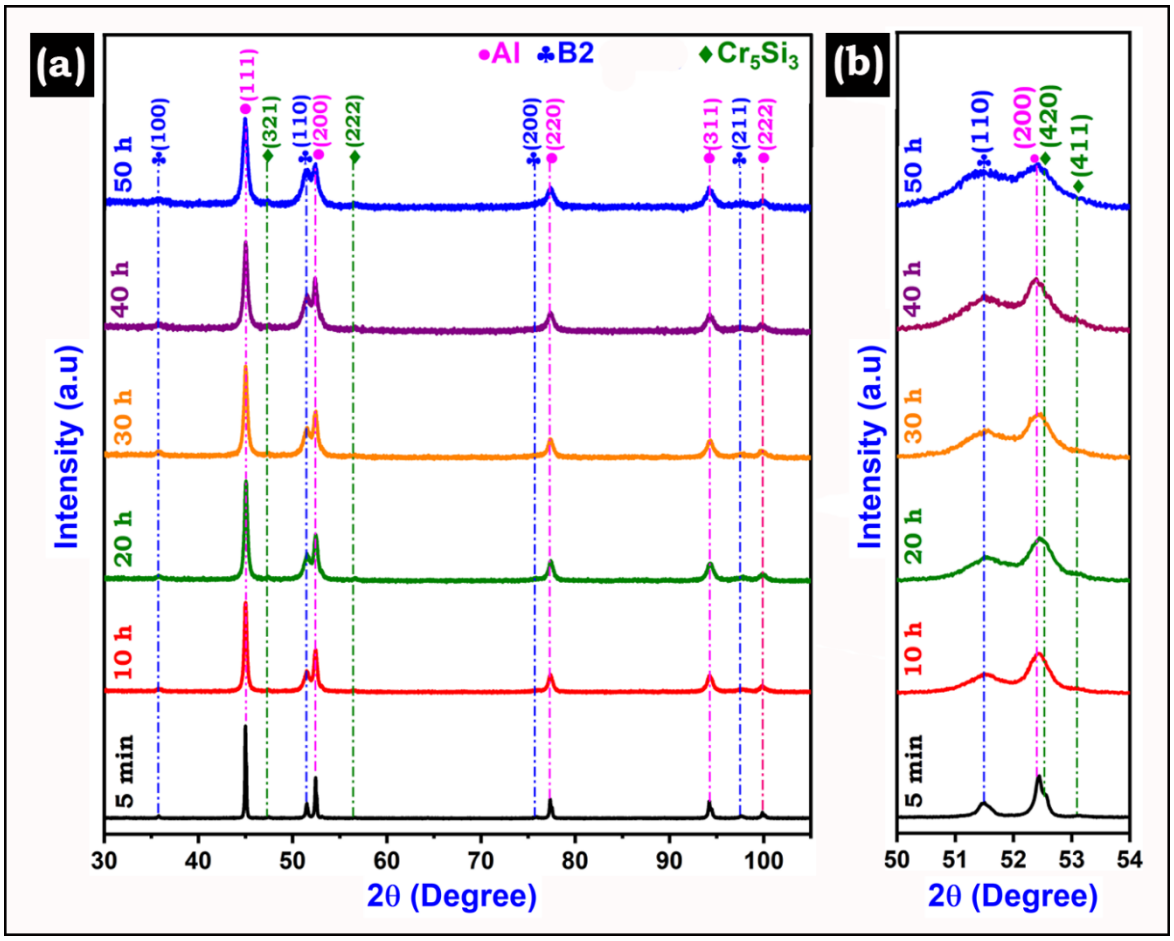

Figure 5. 7: Phase analysis of (a) Al-10HEA nanocomposite powder MM up to 50 h; (b) enlarged image showing co-existence of Al, B2-type and Cr_5Si_3 phase.

5.1.2 TEM investigation of HEA

The structural information and fine microstructural features of the as-cast powdered HEA were ascertained through the TEM micrographs shown in Figure 5.3. The fine powdered HEA particles were used for TEM investigation, and the sample was prepared as per the protocol described in Chapter 2. Figure 5.3 (a) shows the bright-field (BF) image of B2-type HEA particles. The BF image shows a fragmented as-cast B2-type particle having a size ~ 500 nm. A dark region with a size ~ 20-30 nm corresponding to the nanostructured grains is evident from Figure 5.3 (a). The polycrystalline SAD pattern

confirms the presence of a B2-type phase in the non-equiatomic HEA corresponding to the three most intense reflections, i.e., (110), (200), and (211), as observed in Figure 5.3 (b).

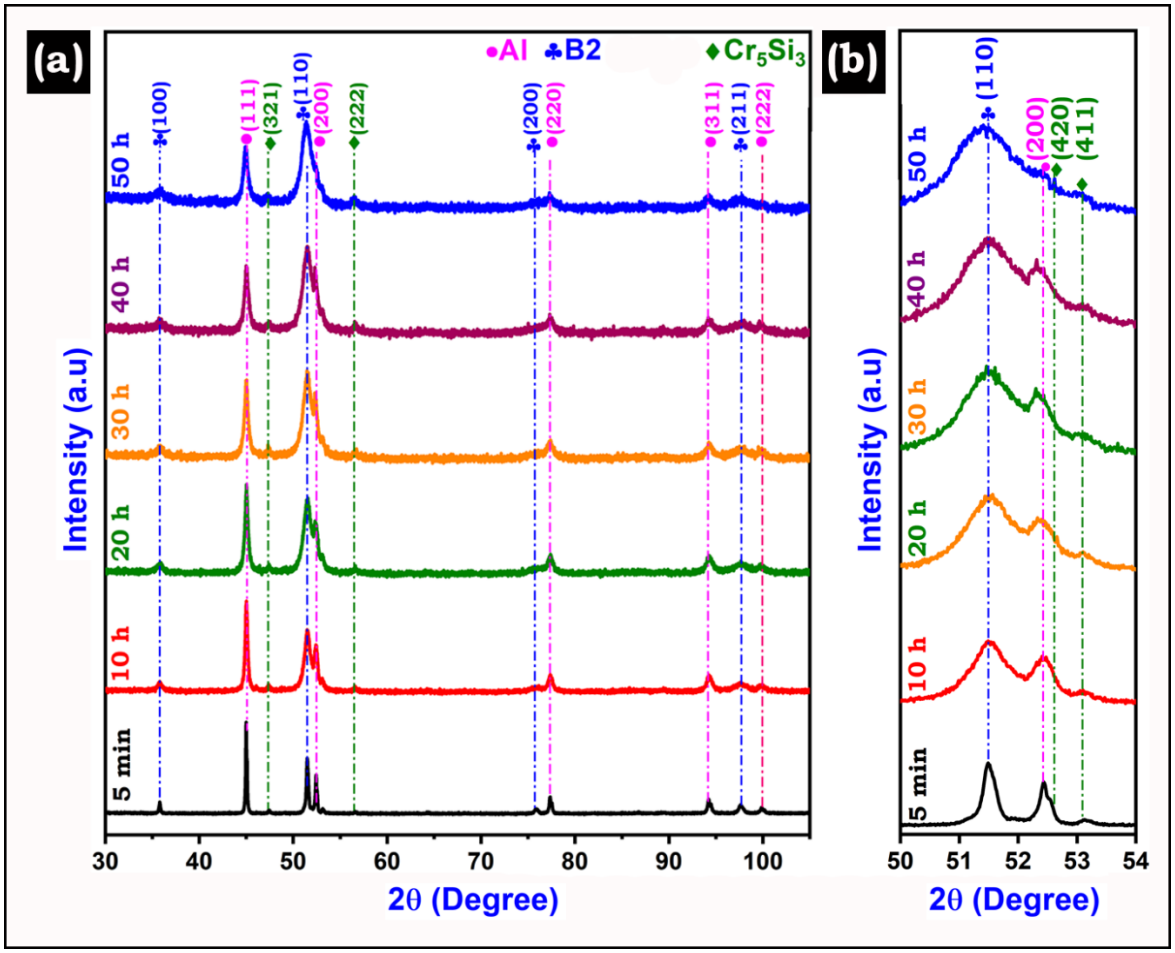

Figure 5. 8: Phase analysis of (a) Al-30HEA nanocomposite powder MM up to 50 h; (b) enlarged image showing co-existence of Al, B2-type and Cr_5Si_3 phase.

.

The faint spot corresponding to the (100) reflection of the B2-type phase marked in Figure 5.3 (b) confirms its ordering and is in line with the XRD pattern of powdered HEA particles (Figure 5.1 (b)). Due to the high intensity of the transmitted beam, only the faint spot corresponding to the (100) reflection of the B2-type phase was observed. The BF image is shown in Figure 5.3 (c) corresponds to the minor Cr_5Si_3 phase present in the as-cast powdered HEA particles. The Cr_5Si_3 phase has a flaky particle attached to the major B2-type phase fine-grained particles. The particle corresponding to the Cr_5Si_3 phase shows

mottled contrast and may due to the processing history of the HEA prepared by melting followed by milling. The SAD pattern is shown in Figure 5.3 (d) further confirms the presence of the Cr_5Si_3 phase in the powdered HEA particles.

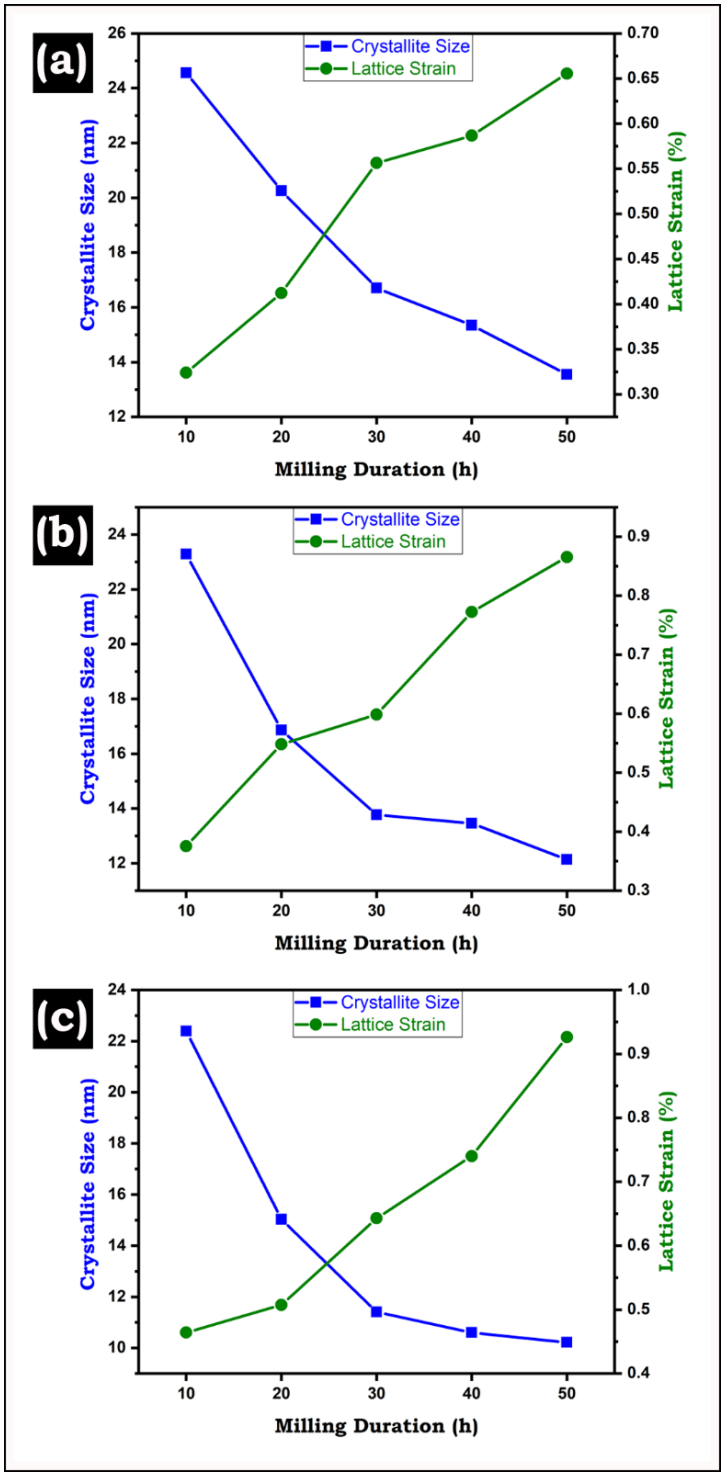

Figure 5. 9: Variation of crystallite size and lattice strain during mechanical milling of (a) Al-10HEA, (b) Al-20HEA, (c) Al-30HEA.

Table 5. 1: Crystallite size, lattice strain, and dislocation density of the Al-HEA nanocomposite powder as a function of milling duration and volume fraction of reinforcement.

Sample designation	Milling Duration (h)	Crystallite Size (nm)	Lattice Strain (%)	Dislocation density $\rho x10^{16}$ (m^{-2})
Al-10HEA	10	25	0.324	3.6
	20	20	0.412	5.6
	30	17	0.556	9.1
	40	15	0.586	10.4
	50	14	0.655	13.2
Al-20HEA	10	23	0.375	4.4
	20	17	0.548	8.9
	30	14	0.598	11.8
	40	13	0.772	15.7
	50	12	0.865	19.5
Al-30HEA	10	22	0.464	5.7
	20	15	0.507	9.2
	30	11	0.642	15.4
	40	11	0.740	19.1
	50	10	0.926	24.8

5.2 Microstructure and morphology of HEA

The microstructural features, morphology, and nominal composition of the as-cast and powdered HEA particles were observed through SEM equipped with EDS. The SEM micrographs shown in Figure 5.4 depicts the microstructure and morphology of the as-cast and powdered HEA particles, respectively. Figure 5.4 (a) shows the microstructure of the

as-cast HEA prepared by melting. It can be discerned that the as-cast microstructure consists of equiaxed grains having a size of around ~10 µm. Precipitates surround these large-sized grains at the grain boundary with a size range of ~2 to 4 µm.

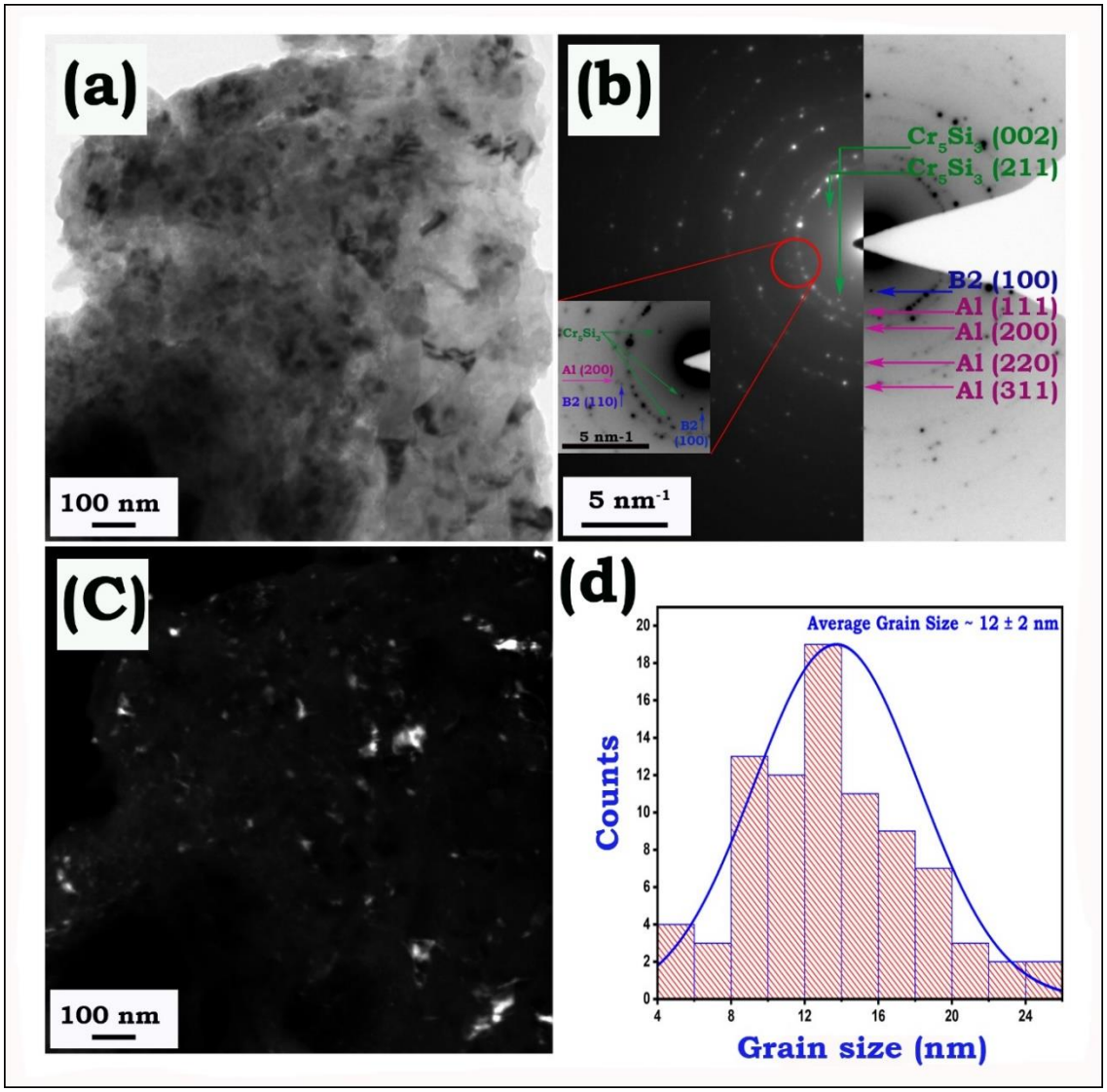

Figure 5. 10: TEM micrograph of Al-30HEA nanocomposite showing the (a) bright-field image (b) corresponding selected area diffraction pattern, (c) dark field image, and (d) grain size distribution in nanocomposites.

For confirming the nominal composition corresponding to the large size grains and the small precipitates, the point EDS analysis of the as-cast samples was done. Figure 5.4 (b) shows the microstructure of the as-cast sample used to evaluate the nominal

composition. The regions selected for discerning large-grained grain and small-sized precipitates chemical composition are marked as EDS spot-1 and EDS spot-2 in Figure 5.4 (b). The nominal chemical composition of the marked regions is mentioned in Table 5.1. It is clear from Table 5.1 that the large grains appearing in Figure 5.4 (a & b) was having a composition close to that of the B2-type HEA. The Al (~ 46 at%) was the major alloying element in the grain, corresponding to the B2-type phase and the other alloying elements. However, the grain corresponding to the B2-type phase was lean in Cr and Si. The small precipitates present at the grain boundary of the B2-type phase are rich in Cr and Si. These precipitates have an elemental composition of Cr ~41 at % and Si ~ 34 at % and other elements like Al, Mn, Fe, and Ni as illustrated in Table 5.1. Further, it was observed that Cu presence in the Cr-Si rich region was negligible. Phase analysis by XRD and SEM can substantiate the two-phase microstructure observed through SEM-EDS analysis.

Table 5. 2: Elemental composition of as – cast non-equiatomic AlSiCrMnFeNiCu HEA.

Elements	**Al**	**Si**	**Cr**	**Mn**	**Fe**	**Ni**	**Cu**
Desired composition	40	10	10	10	10	10	10
Final composition	36.2	8.8	10.9	10.3	11.8	10.3	11.2
EDS spot-1	46.1	4.5	6.4	10.6	11.0	9.6	11.8
EDS spot-2	4.4	34.8	41.5	8.9	5.3	5.1	-

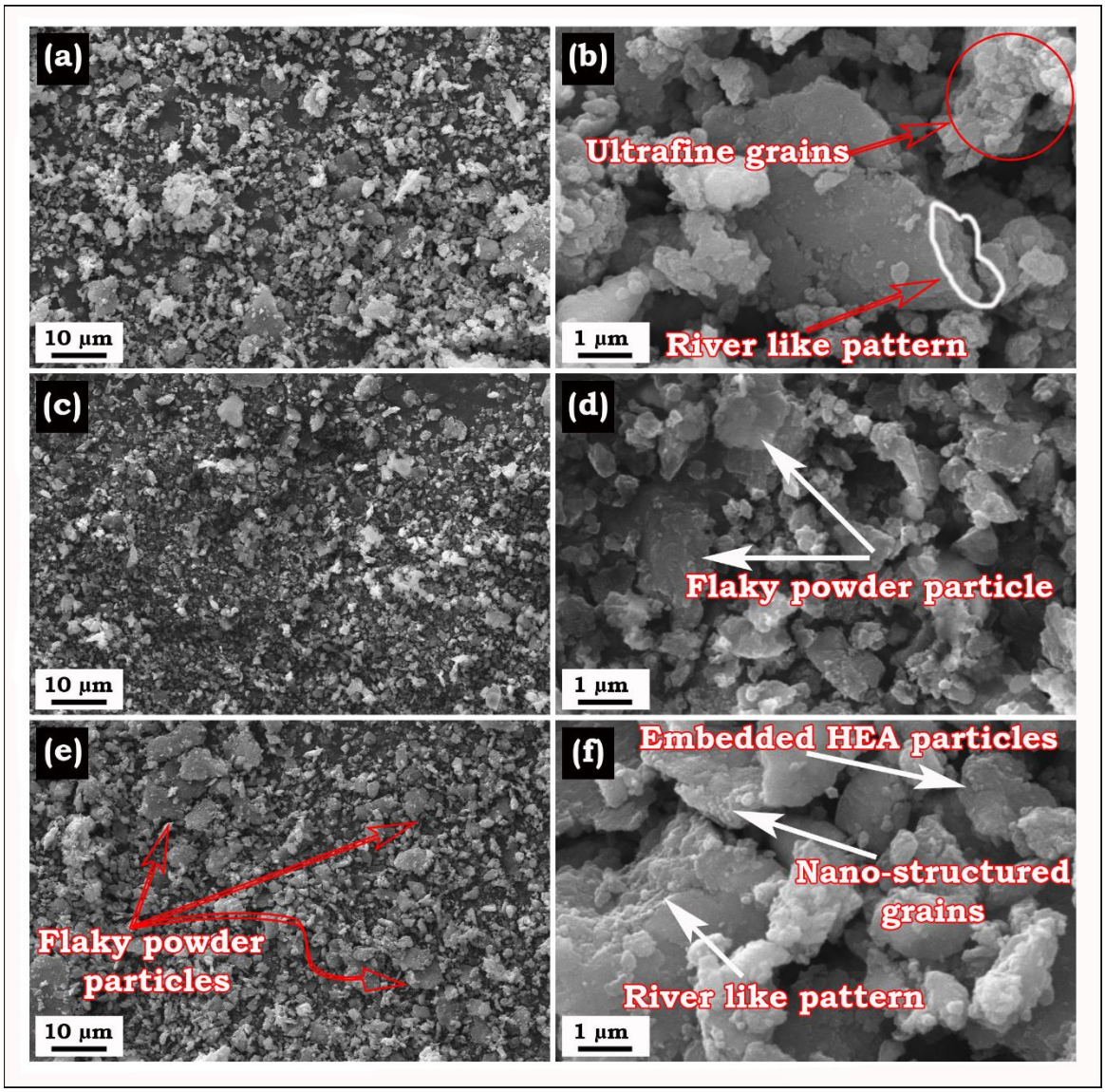

Figure 5. 11: SEM micrograph of Al-HEA nanocomposite powder showing morphology after 50 h of MM in Al-10HEA (a, b), Al-20HEA (c,d), and Al-30HEA at different magnification (e, f).

The morphology of the as-cast powdered HEA particles used as a reinforcement in the AMCs are shown in Figure 5.4 (c). The as-cast HEA fragmented by milling forms the powdered HEA particles through cleavage fracturing as evident from the faceted morphology after milling at a BPR of 100:1. The cleavage fracture in such materials is a normal phenomenon due to their high hardness and inherent room temperature brittleness. Figure 5.4 (d) shows the particle size distribution of the powdered HEA particles prepared

by 30 min of milling. The average particle size was found to be ~ 3.5 ± 0.9 µm. Further, the EDS spectrum of powdered HEA particles and their final composition are shown in Figure 5.4 (e) and Table 5.1 respectively. It is evident from the EDS spectrum that as-cast powdered HEA particles show all the alloying elements with no prominent signature corresponding to oxygen. However, Al minor loss is evident and may be due to the evaporation during melting at high temperatures.

The SEM-EDS elemental mapping of as-cast and powdered HEA are shown in Figures 5.5 and 5.6 respectively. The elemental distribution of the alloying elements used to synthesize as-cast HEA is evident from Figure 5.5. From the SEM-EDS analysis, two distinctive regions lean and rich in Cr and Si were evident. It can be discerned from Figure 5.5, those regions showing high-intensity corresponding to the Cr and Si have low-intensity corresponding to the other elements like Al, Fe, Ni, and Cu. Similarly, the area with high-intensity corresponding to the elements like Al, Fe, Ni, and Cu shows very low intensity for Cr and Si. Further, it was observed from the SEM-EDS mapping that the intensity of Mn was found to be uniform suggesting its homogenous distribution. The powdered HEA particles have a similar kind of elemental distribution as it was observed for the case of as-cast HEA.

5.3 Phase analysis of AMCs reinforced with HEA

The AA 6082 Al matrix nanocomposite reinforced with HEA was synthesized by mechanical milling as per the protocol and parameters described in Chapter 2. The Al-HEA nanocomposite powder was prepared by mechanical milling (MM) up to 50 h. For confirming any structural transformation of the HEA during MM, phase analysis of the nanocomposite powder was done through XRD and TEM investigation.

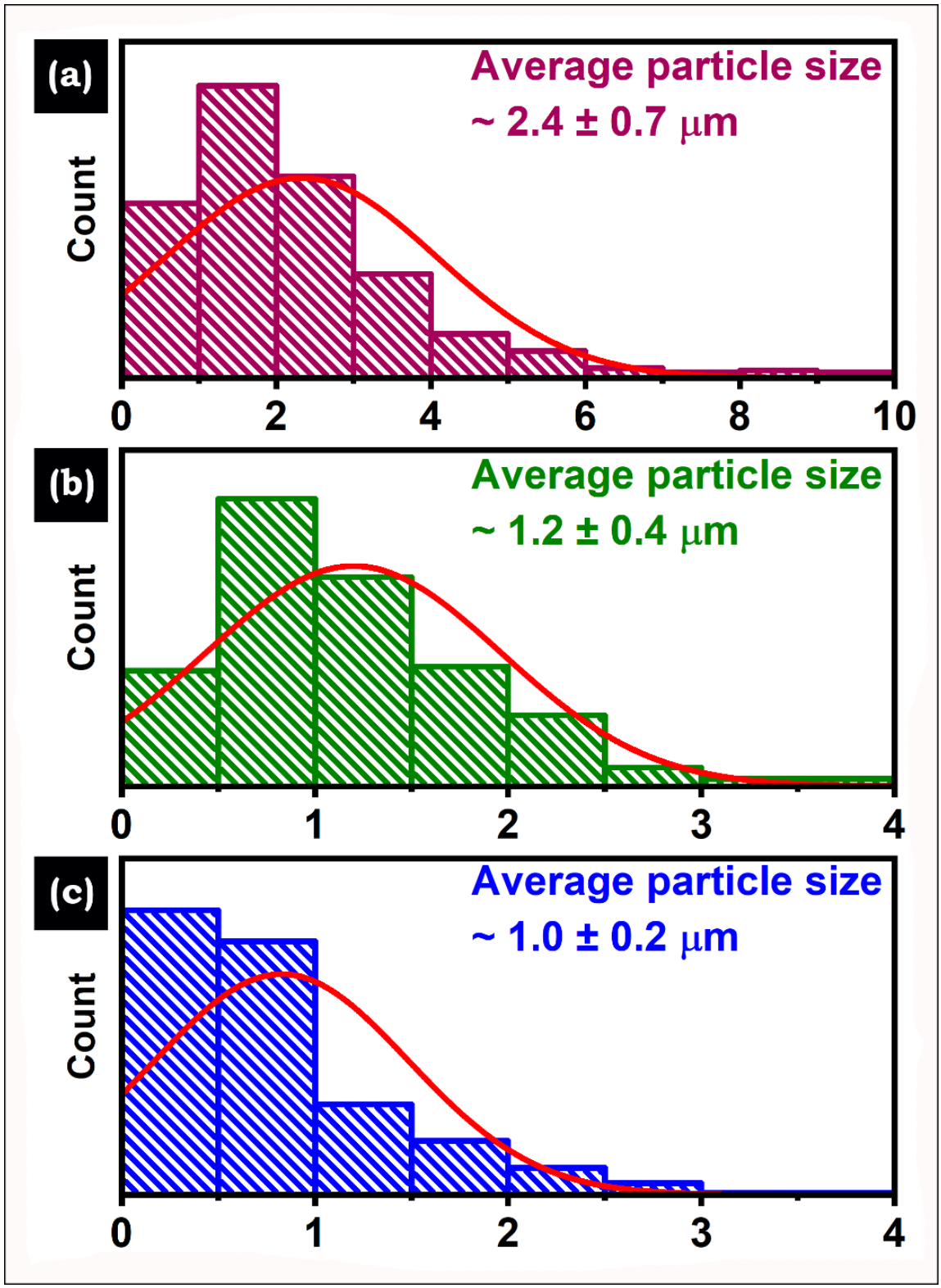

Figure 5. 12: Particle size distribution of (a) Al-10HEA (b) Al-20 HEA and (c) Al-30HEA nanocomposite powder mechanically milled up to 50 h.

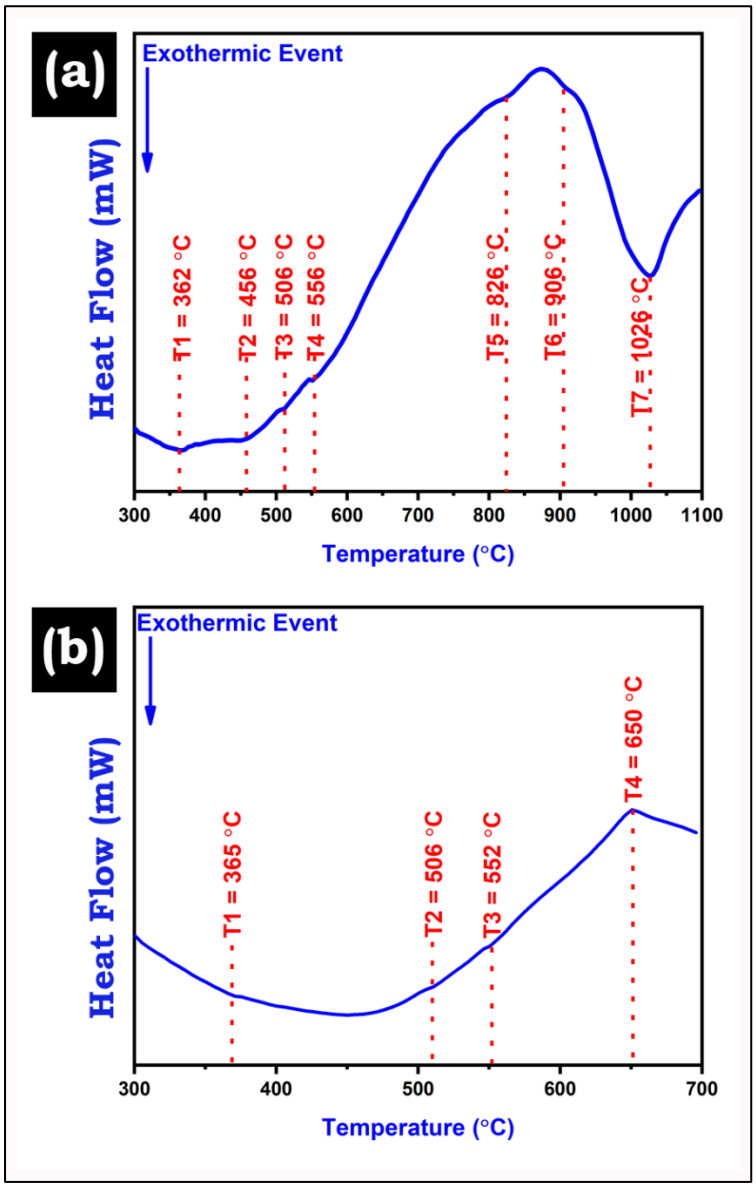

Figure 5. 13: DSC thermogram of (a) as-cast powdered non-equiatomic HEA; (b) Al-30HEA nanocomposite at a 20 K/min scan rate.

5.3.1 XRD of Al-HEA nanocomposite powder

The Al-HEA nanocomposite powder was MM up to 50 h, with the varying volume fraction of HEA particles. Detailed phase analysis by XRD was done for ascertaining any structural transformation of either the Al matrix or the HEA reinforcement during 50 h of MM. The phase analysis of Al-10HEA and Al-30HEA nanocomposite powder was shown in Figures 5.7 and 5.8, respectively.

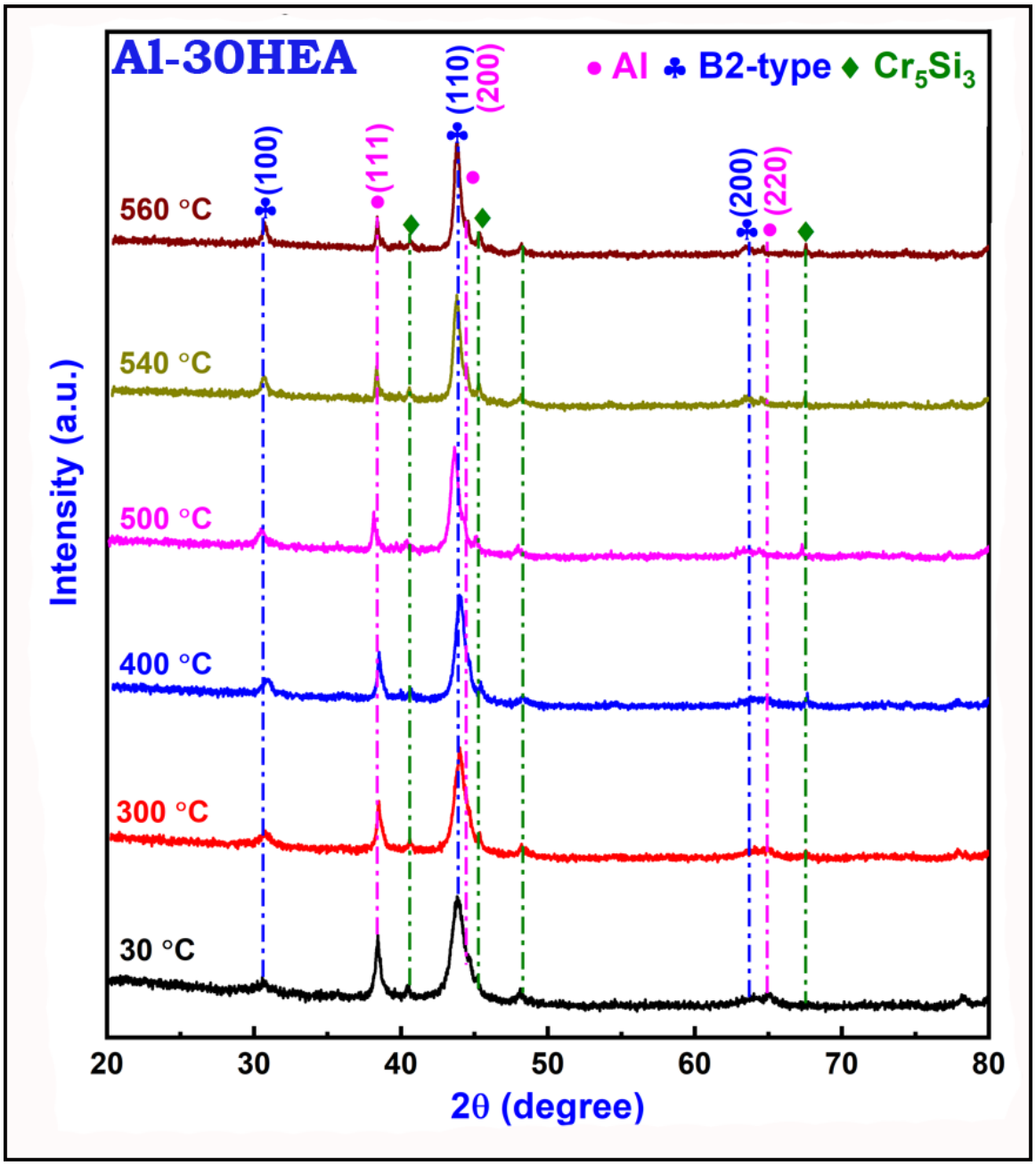

Figure 5. 14: In-situ XRD pattern (λ=0.15402 nm) of Al-30HEA at high temperatures.

It was observed that even after varying the volume fraction of reinforcement from 10 to 30 vol%, no changes in the Al matrix was observed. During MM up to 50 h, the starting AA 6082 Al matrix shows the presence of all reflections of FCC-Al (a=0.40494 nm) having all primary reflections, i.e. (111), (200), (220), (311) and (222). During the milling of Al-HEA nanocomposite powder, no structural transformation of the B2-type

major and Cr_5Si_3 minor phases was observed, as illustrated in Figure 5.7 (a & b) and 5.8 (a & b). Figure 5.7 (b) and 5.8 (b) show the enlarged image showing the co-existence of Al, B2-type phase, and Cr_5Si_3 phase for Al-10HEA and Al-30HEA respectively. Even after MM for 50 h, the B2-type major phase was able to retain its ordered structure as discerned from Figure 5.7 (a) and 5.8 (a), showing the existence of (100) reflection in Al-10HEA and Al-30HEA having a d-spacing ~0.290 nm respectively. It can be discerned from these figures that the intensity of (202) reflection of the Cr_5Si_3 phase diminishes after 10 h of MM regardless of the volume fraction of HEA particles in the Al matrix. The asymmetric peak of (202) reflection of Cr_5Si_3 having a d-spacing ~0.2069 nm associated with the (110) peak of B2-type phase in the as-cast and powdered HEA samples was no more evident in the Al-10HEA and Al-30HEA as illustrated in Figure 5.7 (b) and 5.8 (b) respectively. Further, the (413) reflection of Cr_5Si_3 was also not able to retain its identity even after 10 h of MM for Al-10HEA and Al-30HEA. It can be inferred from Figure 5.7 and 5.8 that no sign of the structural transformation of Al-HEA nanocomposite powder was evident as a function of volume fraction of reinforcement and mechanical milling duration.

Significant broadening and peak shift of the corresponding to the planes of Al matrix was evident from Figure 5.7 and 5.8. On increasing the volume fraction of HEA particles, the broadening of peaks corresponding to the Al matrix was found to increase. The broadening and peak shift of the Al matrix may be correlated with the crystallite size and lattice strain. The variation of crystallite size and lattice strain as a function of milling duration and volume fraction of HEA particles is observed from Figure 5.9 and reported in Table 5.2. The increase in the volume fraction reinforcement enhances the crystallite size refinement and considerably increases its lattice strain. The crystallite size for Al-10HEA, 20HEA and 30HEA was found to be ~14 nm, 12 nm, and 10 nm, respectively, for the Al

matrix MM for 50 h. The lattice strain of these Al matrices was also found to be significant and varied from 0.655% for Al-10HEA to 0.926% for Al-30HEA, as reported in Table 5.2. This considerable crystallite size refinement and exorbitant rise in the lattice strain can be attributed to the hard HEA particles having a major B2-type and minor Cr_5Si_3 phase. It can be observed from Figure 5.9 that the reduction in crystallite size is very significant up to 30 h of MM. However, after 30 h of MM, the level of crystallite size refinement for Al-10HEA, 20HEA, and 30 HEA was not significant as indicated in Table 5.2. During MM initial stages, the Al-HEA powder particles entrapped between the colliding WC balls experience a high impact, and the balls kinetic energy is transferred to them. Therefore, the Al-HEA nanocomposite powder undergoes a high dislocation density leading to its work hardening. The dislocation density of the Al-HEA nanocomposite powder was found to increase as a function of volume fraction of reinforcement and duration of MM. However, the crystallite size reduction and increase in the lattice strain and dislocation density are not very significant after 30 h of MM. During prolonged duration of MM, the rate of plastic deformation usually reduces the extent of an increase in the dislocation density, as evident from Table 5.2. Therefore, the crystallite size refinement and increase in the lattice strain after 30 h of Al-HEA nanocomposite powder after 30 h of MM were not very appreciable.

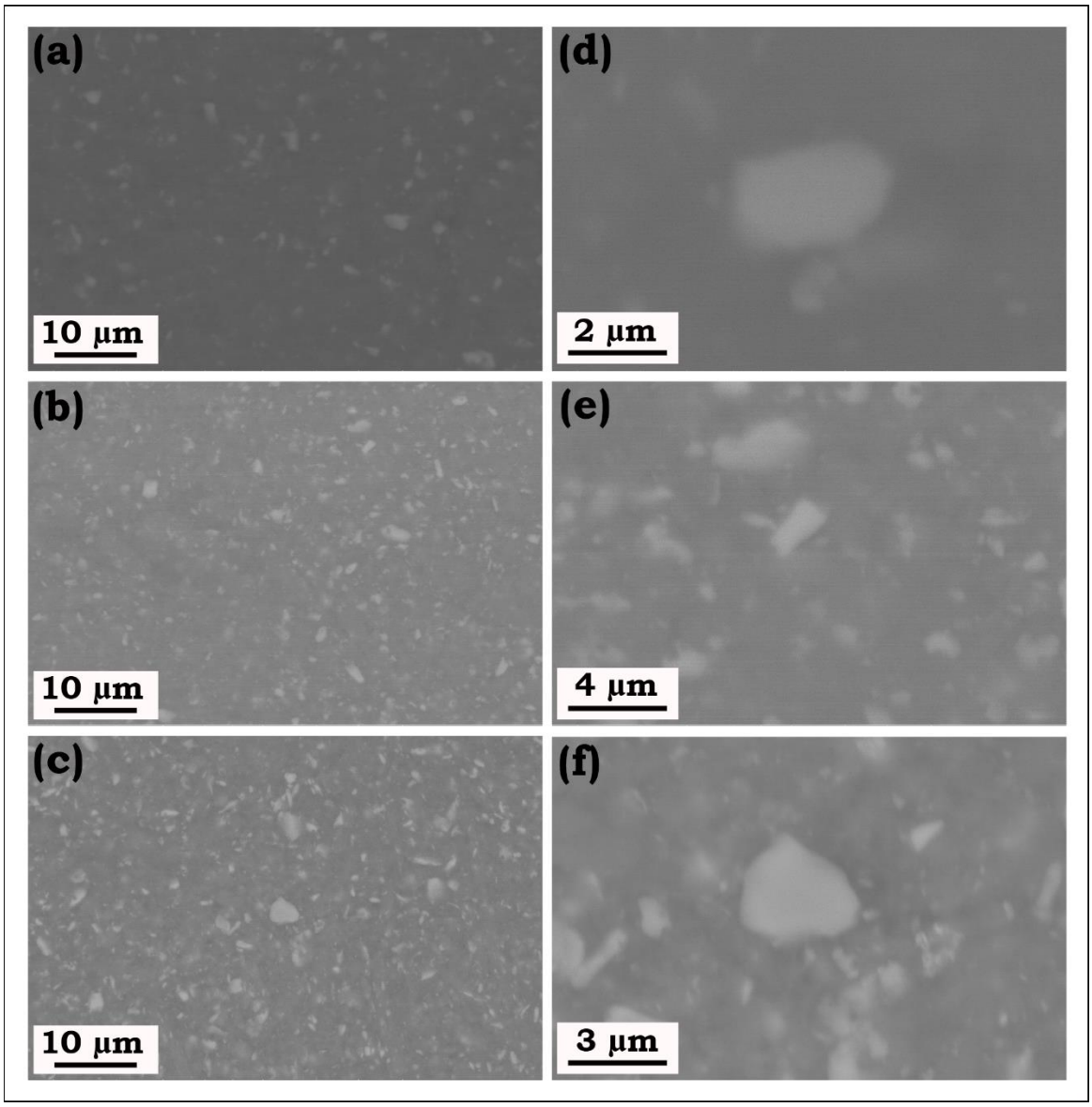

Figure 5. 15: SEM micrograph of (a & d) Al-10HEA, (b & e) Al-20HEA, (c & f) Al-30HEA consolidated by pressure-less sintering.

5.3.2 TEM investigation of Al-HEA milled powder

The diffraction contrast images of Al-30HEA nanocomposite powder MM up to 50 h are shown in Figure 5.10 (a-c). The bright-field (BF) image and corresponding selected area diffraction (SAD) pattern along with the dark field (DF) image are shown in Figure 5.10 (a), 5.10 (b), and 5.10 (c), respectively for Al-30HEA nanocomposite powder. In Al-

30HEA, many dark patches corresponding to non-equiatomic HEA particles and strain accumulation are observed in the BF image shown in Figure 5.10 (a).

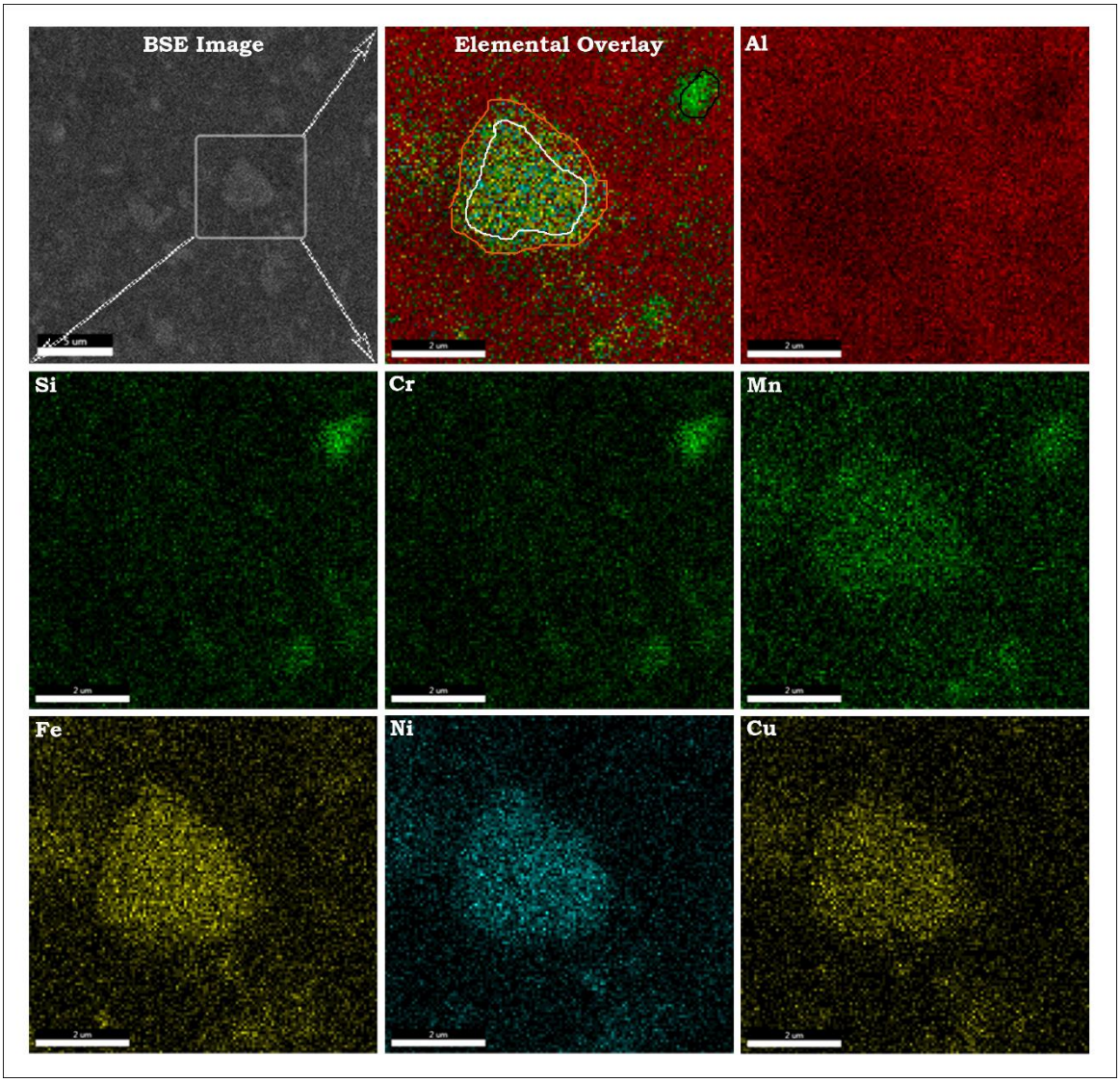

Figure 5. 16: SEM-EDS mapping of Al-30HEA composite consolidated by pressure-less sintering.

The dark region in Al-30HEA can be discerned due to enhanced grain refinement during severe plastic deformation of the Al matrix in the presence of hard non-equiatomic AlSiCrMnFeNiCu HEA particles. The polycrystalline nature of the SAD pattern, as shown in Figure 5.10 (b) discerns the random crystallographic texture and nanostructuring of the Al matrix in the Al-30HEA nanocomposite powders. The careful observation of the SAD

pattern shows the presence of B2-type and Cr_5Si_3 phase along with the rings corresponding to the (111) plane of Al.

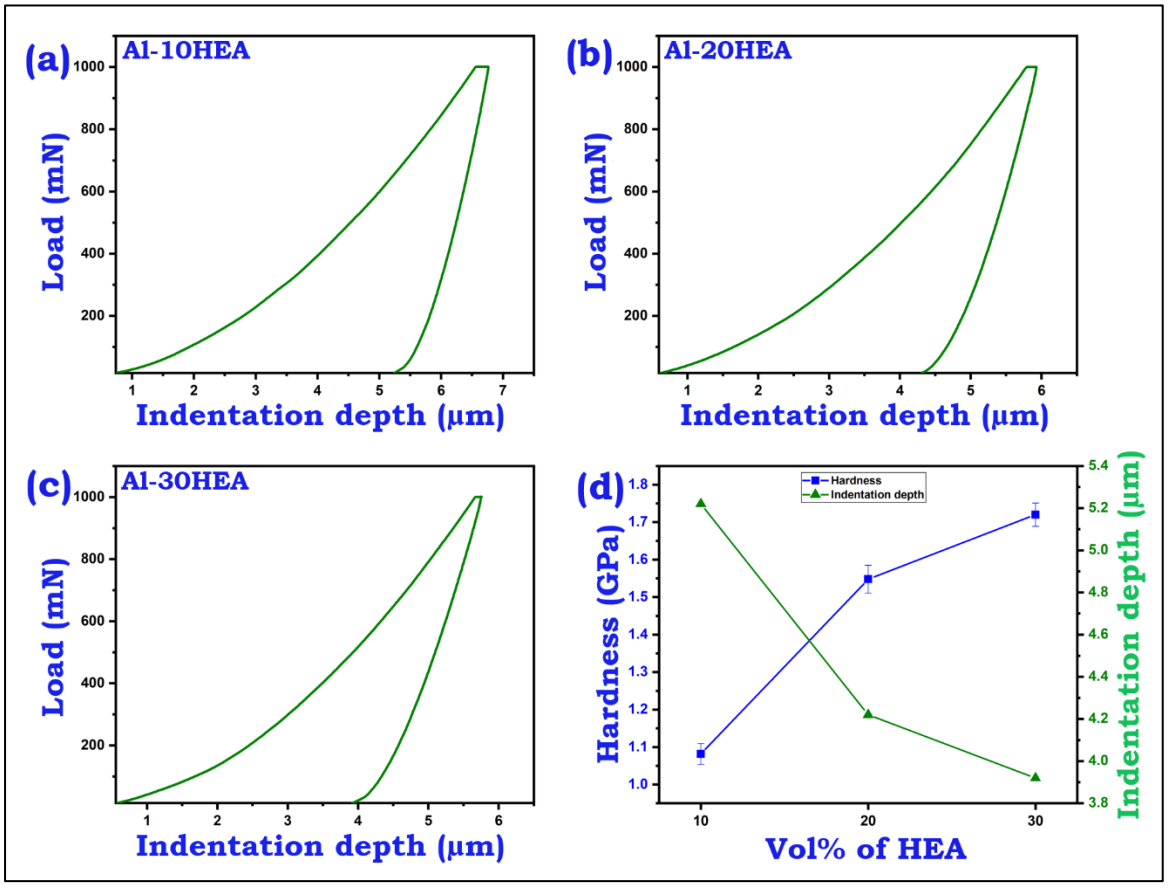

Figure 5. 17: Load versus indentation depth plot for (a) Al-10HEA (b) Al-20HEA and (c) Al-30HEA composite; (d) variation of hardness and depth of indentation as a function of volume fraction of HEA reinforcement in Al-HEA pressure-less sintered composite.

The inset in Figure 5.10 (b) shows the presence of (100) and (110) plane of B2-type phase having a d-spacing ~0.290 nm and ~0.2056 nm respectively. The SAD pattern is shown in Figure 5.10 (b) further confirms the presence of (211) and (002) reflection of Cr_5Si_3 phase having d-spacing ~0.3070 nm and 0.2319 nm. The B2-type phase in HEA having interplanar spacing d ~ 0.2056 nm, is very close to that of the (200) reflection of α-Al (d ~ 0.2024 nm). The co-existence of reflection corresponding to the Al matrix and HEA particles was also evident from the powder XRD pattern of Figure 5.7 and 5.8. The DF image shows the formation of a nanostructured grain ~12 nm by extensive deformation

during the repetitive fracturing and cold welding of Al-HEA as evident from the Figure 5.10 (c) and grain size distribution shown in Figure 5.10 (d). The size of the nanostructured grains formed after 50 h of MM, observed through TEM, may be substantiated by the crystallite size of the Al matrix in Al-HEA composite, as evident from Table 5.2. The grain refinement observed through TEM is in line with the XRD findings showing the crystallite size ~10 nm for Al-30HEA nanocomposite powder MM for 50 h.

Table 5. 3: Hardness of Al-HEA pressure-less sintered composite.

Sample designation	Hardness (GPa)	Depth of indentation (μm)	Hardness (HV)	Estimated Yield Strength (MPa)
Al-10HEA	1.10	5.22	104	312
Al-20HEA	1.51	4.22	142	426
Al-30HEA	1.72	3.92	162	486

5.4 Morphology of Al-HEA milled powder

The morphology of the AA 6082 Al matrix nanocomposite reinforced with HEA particles is shown in Figure 5.11 (a – f). It is evident from Figure 5.11 (a), (c), and (e) that for Al-10HEA, 20HEA, and 30HEA that on increasing the volume fraction of HEA particles, the tendency for refinement of the Al matrix increases. The particle size refinement enhancement was also evident from the particle size distribution shown in Figure 5.12. The improvement level was maximum for Al-30HEA nanocomposite powder, having a particle size of ~1.0±0.2 μm. It is evident from Figure 5.11 (a, c, e) that both the flaky and equiaxed morphology of milled powder after 50 h of MM was observed. The particle with flaky morphology is formed during MM initial duration and can be attributed to the extensive deformation of the soft Al matrix in the nanocomposite powder. However,

the equiaxed particle morphology is evident when the MM process reached a steady state. The hard non-equiatomic reinforcement particles further contribute to the fragmentation and nanostructuring of the soft Al matrix. Therefore, after 50 h of milling, the particles are equiaxed and a few flaky particles were observed in Al-HEA nanocomposite powder. Further, it can be discerned from the Figure 5.11 (b), (d), and (f) for Al-10HEA, 20HEA, and 30HEA that the increase in the volume fraction of HEA particle also enhances the nanostructuring of the ductile Al matrix. From Figure 5.11 (b), ultrafine grains and river-like pattern were observed. However, increasing the HEA particles in Al-30HEA shown in Figure 5.11 (f) the nanostructured grain was observed, and the thickness of the river like pattern increases. Further, it can be discerned that the HEA particles are well embedded in the ductile Al matrix with good interfacial bonding for the case of Al-30HEA nanocomposite powder. This can be attributed to the change in MM mechanism due to the increase in hard non-equiatomic HEA particles, enhancing the fragmentation and refinement of the Al matrix during milling.

5.5 Thermal stability of Al-HEA milled powder

The thermal stability of the powdered HEA particles and the Al-30HEA nanocomposite powder was established through DSC at a scan rate of 20 K/min, as shown in Figure 5.13. The Figure 5.13 (a) shows seven exothermic peaks at T1 ~ 362 ℃, T2 ~ 456 ℃, T3 ~ 506 ℃, T4 ~ 556 ℃, T5 ~ 826 ℃, T6 ~ 906 ℃, and T7 ~ 1026 ℃ for powdered HEA particles. The Figure 5.13 (b) shows the four (04) exothermic peaks at T1 ~ 365 ℃, T2 ~ 506 ℃, T3 ~ 552 ℃, and one (01) endothermic peak at T4 ~ 650 ℃ for Al-30HEA nanocomposite powder. However, the exothermic peak in Figure 5.13 (a) at T1 until T6 are very negligible. Similarly, for Al-30HEA nanocomposite powder, the exothermic peaks at T1 until T3 were also very negligible, as shown in Figure 5.13 (b).

The endothermic peak at T4 can be attributed to the Al-HEA nanocomposite powders melting of the Al matrix. Similarly, the powdered HEA was found to be stable up to 1026 ℃ (1299 K). For co-relating, the exothermic peaks with any structural transformation, in-situ XRD of Al-30HEA nanocomposite powder was carried out at 30 ℃ (300 K), 300 ℃ (573 K), 400 ℃ (673 K), 500 ℃ (773 K), 540 ℃ (813 K), and 560 ℃ (833 K) as evident from Figure 5.14. It can be discerned from Figure 5.14 that the till 560 ℃ (833 K) no structural transformation of the Al matrix, B2-type and Cr_5Si_3 phase in HEA was observed. This established the thermal stability of Al-30HEA nanocomposite powder up to 560 ℃ (833 K).

5.6 Pressure-less sintering of Al-HEA composite

The Al-HEA composite was consolidated by pressure-less sintering method at 560 ℃ (833 K) for 4 h, followed by furnace cooling. For pressure-less sintering, the green compacts of Al-HEA powder were sealed in a quartz tube back-filled with Ar gas, and the detailed procedure is described in Chapter 2. The pressure-less sintered Al-HEA composite has the same phase as observed during the in-situ XRD of nanocomposite powder at 560 ℃ (833 K). The back-scattered electron (BSE) SEM micrograph of Al-10HEA, 20HEA, and 30HEA are shown in Figure 5.15 (a & d), (b & e), and (c & f) respectively, at different magnification. It is observed from Figure 5.15 (a), (b), and (c) that the HEA reinforcement is homogeneously dispersed in the Al matrix. From Figure 5.15 (d), (e), and (f) two distinctive contrast, namely light grey and dark grey contrast was observed in Al-10HEA, 20HEA, and 30 HEA, respectively. The phases corresponding to these contrast were observed from the elemental analysis of these regions through SEM-EDS techniques.

Table 5. 4: Chemical enthalpy of mixing (ΔH^{mix}_{ij} , kJ/mol) of atomic pairs for non-equiatomic AlSiCrMnFeNiCu HEA alloy following the Miedema's approach [404–406].

Element	Al	Si	Cr	Mn	Fe	Ni	Cu
Al	-	-19	-10	-19	-11	-22	-1
Si	-19	-	-37	-45	-35	-40	-19
Cr	-10	-37	-	2	-1	-7	12
Mn	-19	-45	2	-	1	-2	13
Fe	-11	-35	-1	1	-	-8	4
Ni	-22	-40	-7	-2	-8	-	4
Cu	-1	-19	12	13	4	4	-

Table 5. 5: Calculate thermodynamic and physical parameter of non-equiatomic AlSiCrMnFeNiCu HEA.

ΔH_{mix} $\left(kJ/mol\right)$	ΔS_{mix} $\left(\frac{JK^{-1}}{mol}\right)$	Tm (K)	Ω	δ (%)	VEC
-19.48	14.53	1404	1.05	5.75	5.8
VEC is Valence electron concentration; δ is atomic size difference; Ω is omega parameter					

It was ascertained that the dark grey contrast has an elemental composition close to that of the Al matrix. However, the light grey contrast has an elemental composition close to that of the non-equiatomic HEA particle. Further, it can be observed that the interfaces

in Al-HEA composite are not sharp; instead was found to be diffused in nature. This kind of interface establishes the good interfacial bonding between the Al matrix and HEA reinforcement particles. The diffused nature of interfaces in the Al-30HEA composite was observed through the SEM-EDS mapping as illustrated in Figure 5.16. The BSE-SEM micrograph depicts the presence of two types of particles, as explained previously. The SEM-EDS mapping discerns the presence of both the major B2-type and minor Cr_5Si_3 phase of HEA particles in the Al matrix. The quasi-spherical particle with a size of ~2.0 µm, whose boundary is marked with the white colour, was close to the elemental composition of the B2-type phase. The intensity of elements like Al, Mn, Fe, Ni and Cu was found to be high in this region. Apart from this, the small-elongated type of particle whose boundary is marked with black colour in the elemental overlay was found to have high-intensity corresponding to the elements like Cr and Si. In the region having a high intensity of Cr and Si was also has considerable intensity corresponding to that of the Mn. Therefore, it can be inferred that the Mn is present in both the B2-type and Cr_5Si_3 phase. Similar to the diffused interfaces seen in Figure 5.15, a transition layer between the Al matrix and major B2-type phase of HEA was observed in the SEM-EDS mapping demarcated by the orange line seen on the micrograph showing elemental overlay. The thickness of the transitional layer (between the white and orange line) was found to be in the range of 400 to 500 nm, as observed from Figure 5.16. Apart from the transition layer, the elements like Fe, Ni, and Cu was found to be present in the Al matrix as illustrated through the SEM-EDS mapping.

The microhardness of Al-HEA pressure-less sintered composite was evaluated through instrumented indentation techniques as per the procedure described in Chapter 2. The load versus indentation depth curve for Al-10HEA, 20HEA and 30HEA was shown in

Figure 5.17 (a), (b), and (c) respectively at a load of 1000 mN, to observe the contribution due matrix and reinforcement in the composite.

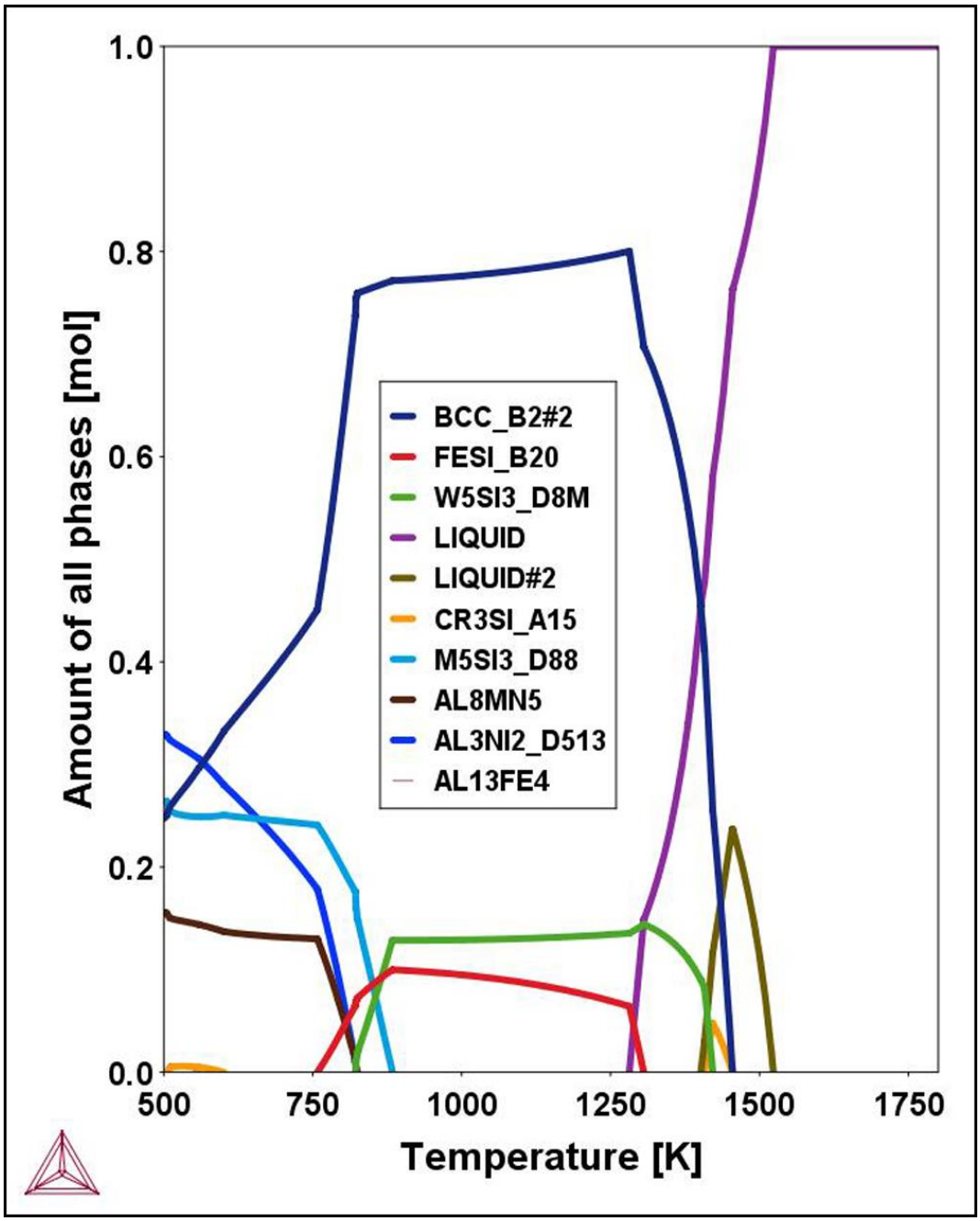

Figure 5. 18: Property diagram for non-equiatomic AlSiCrMnFeNiCu HEA by ThermoCalc.

The microhardness and the depth of indentation in mentioned in the Table 5.3. It can be observed from the Table 5.3 and Figure 5.17 (d) that on increasing the volume

fraction HEA reinforcement in Al matrix, the microhardness increases considerably and depth of indentation decreases to ~1.72 GPa and 3.92 µm. The yield strength (YS) of the Al-HEA composite was calculated using Tabor's equation (yield strength = 3*hardness (in HV)) as described by Shivam et al. [407]. The YS of the Al-10HEA, 20HEA and 30HEA was found to be ~312 MPa, 426 MPa, and 486 MPa, respectively, as mentioned in Table 5.3. This high value of microhardness and YS can be attributed to the homogenous distribution of hard non-equiatomic HEA particles and the formation of a transitional layer and solid solution strengthening due to alloying elements in the Al matrix subjected to pressure-less sintering.

5.7 Discussion

The present work addresses the exploitation of non-equiatomic AlSiCrMnFeNiCu HEA as a reinforcement material for designing lightweight, high strength AMCs for structural application. The non-equiatomic HEA with Al as the principal alloying elements have shown high hardness and good strength at room temperature and high temperature [408–414]. These non-equiatomic HEA properties can be exploited as reinforcements in AMCs to engineer the interfaces of Al-matrix and HEA particles. It is of utmost importance to study the phase evolved in non-equiatomic AlSiCrMnFeNiCu HEA, their reinforcement in AMCs, and Al-HEA composite interfaces.

5.7.1 Phase evolution in HEA

The phases evolved during vacuum induction melting of $Al_{40}(SiCrMnFeNiCu)_{60}$ (at %) HEA can be explained based on a few thermodynamic parameters. The binary mixing enthalpy (ΔH_{mix}) of alloying elements used for the synthesis of non-equiatomic HEA is mentioned in Table 5.4. From Table 5.4, it can be discerned that the mixing enthalpy for a few binary systems are highly negative, i.e., Cr-Si (-37 kJ/mol), Mn-Si (-45 kJ/mol), Fe-Si

(-35 kJ/mol). Apart from these binary, comparatively less negative enthalpy of mixing was also observed for Al-Si (-19 kJ/mol), Al-Mn (-19 kJ/mol), Al-Fe (-11 kJ/mol), Al-Ni (-22 kJ/mol) systems. This negative enthalpy of mixing surge the formation of intermetallic phases in equiatomic and non-equiatomic HEA [408–415]. Therefore, the non-equiatomic AlSiCrMnFeNiCu HEA was found to be consisting of a major B2-type and a minor Cr_5Si_3 phase as illustrated in Figure 5.1 until 5.4.

A few other thermodynamic and physical parameters are reported in Table 5.5. A study by Zhang et al. [416] have proposed three necessary criteria for the formation of disordered solid solution phase as (i) -10 kJ/mol<ΔH_{mix}<5 kJ/mol, (ii) ΔS_{conf} > 13.38 kJ/mol, (iii) δ<4%. The highly negative enthalpy of mixing (-19 kJ/mol) and large atomic size difference 'δ' (~5.8 %) led to the formation of an ordered BCC phase and minor phase corresponding to Cr_5Si_3. Apart from the conditions proposed by Zhang et al. [416], Guo and Liu et al. [417] have suggested two parameters, namely electronegativity and valence electron concentration (VEC), for the formation of a single-phase solid solution. For VEC>8.0, 6.87<VEC<8.0 and VEC<6.87 results in the evolution of FCC, FCC, and BCC, and BCC structure, respectively. VEC's values are mentioned in Table 5.5 and were found to be ~5.8, suggesting phase formation with a BCC crystal structure. Although the non-equiatomic HEA satisfies the criteria laid by Guo and Liu, however, ordered BCC phase was found to form instead of the disordered BCC phase. Yang and Zhang [418] proposed two parameters 'δ' and 'Ω', to develop a disordered solid solution that should be <6.6 % and >1.1, respectively. The value of 'Ω' is 1.05, which is not within the limit for solid solution formation as seen in the Table 5.5. Therefore, in the present investigation, two phase HEA having a major B2-type and minor Cr_5Si_3 phase was formed after vacuum induction melting of non-equiatomic HEA.

A similar observation was made from the property diagram generated by Thermo-Calc software, as shown in Figure 5.18. The liquidus line of the molten alloy starts at ~ 1550 K and end at ~1280 K. The solidus line of B2-type phase starts at ~1450 K. It reaches a maximum at ~1280 K. Similarly, the solidus line of Cr_5Si_3 phase starts at ~1400 K. It reaches maximum at ~ 1300 K. It can be discerned from the Figure 5.18, that the B2-type phase and Cr_5Si_3 phase was found to form and has a phase fraction of ~85% and 15% respectively at ~1280 K. However, the phase fraction observed for B2-type and Cr_5Si_3 type phase slightly vary with the findings of XRD. This can be attributed to the fact that the property diagram usually shows phases under equilibrium conditions. However, in the present work, the molten HEA alloy was poured onto a copper crucible leading to a faster cooling, which is supposedly not an equilibrium condition. From the various thermodynamic parameters and the property diagram computed by Thermo-Calc software, it can be discerned that the formation of a single-phase solid solution is evitable. The property diagram findings generated by Thermo-Calc software are in line with experimentally observed phases after the vacuum induction melting of non-equiatomic HEA.

A few researchers studied the effect of Al addition on the phase evolution of HEA containing 3d transition elements [408–415]. In an investigation, Zhao et al. [203] have studied the effect of Al and Ti addition in $Al_{2-x}CoCrFeNiTi_x$ non-equiatomic HEA. They have reported the formation of a BCC phase and B2 phase enriched in Fe-Cr and Ni-Al, respectively for $Al_2CoCrFeNi$ HEA. In another study, Zhao et al. [199] have reported the formation of BCC phase and B2-type phase enriched in Fe-Cr and Ni-Al respectively for HEA having a nominal composition of $Al_{1.6}CrCo_{0.4}FeNi$. Similarly, Feuerbacher [204] observed the formation of a B2-ordered phase with a small BCC inclusion for non-

equiatomic HEA with a nominal composition of $Al_{28}Co_{20}Cr_{11}Fe_{15}Ni_{26}$ (at%). The $Al_{2.75}CoCrFeNi$ HEA was found to have disordered BCC and ordered BCC phases, as evident from the study of Aizenshtein et al. [201]. Recently, Liu et al. [207] have reported the variation in the phase formed w.r.t to a fraction of Al and Ni in $Al_xCo_{15}Cr_{15}Ni_{70-x}$ HEA. They have said the formation of $L1_2$ and B2-type phase for 19.5 to 27.5 at% of Al. However, increasing the Al in the HEA to 35 at% results in forming a single ordered BCC phase.

On contrary to this a few researches and co-workers have demonstrated the formation single B2-type phase in $Al_xCoCrCuFeNi$ ($x \geq 3.0$ mol or 37.5 at%) [408,409,411,412]. In an investigation, Jin et al. [410] have reported BCC/ B2 phase formation and minor phases of Cr_3Si for HEA with a nominal composition of $Al_2CoCrFeNiSi$. Similarly, Singh et al. [344] have reported the formation of the Cr_5Si_3 silicide phase in MgAlSiCrFe HEA annealed above 600 ℃ (873 K). It is clear that for $x \leq 3.0$-mole fraction in $Al_xCoCrFeNi$ HEA, the microstructure consists of a B2-type phase along with a disordered BCC phase. In almost all the cases, the BCC phase is enriched in Fe and Cr, and the B2-type phase is enriched in Ni and Al. However, in the present investigation, due to the high negative enthalpy Cr-Si, favors the formation of Cr_5Si_3 type phase and the propensity of Fe and Cr enriched BCC phase becomes negligible. Therefore, in the present investigation, the B2-type phase was found to be enriched in both Ni and Fe. Based on the current understanding from literature, thermodynamic parameters, and property diagram generated from Thermo-Calc software, it can be discerned that the formation of B2-type phase long with minor phases corresponding to Cr_5Si_3 is possible for AlSiCrMnFeNiCu non-equiatomic HEA.

5.7.2 Microstructural features and mechanical properties of Al-HEA composite

In the present work, considerable efforts were made to investigate the interfaces and their effect on the mechanical properties of age-hardened 6082 Al matrix composite reinforced with non-equiatomic AlSiCrMnFeNiCu HEA particles through pressure-less sintering. For investigating any possible interfacial reactions in Al-HEA composite, the thermal analysis of nanocomposite powder was conducted. The minor exothermic fluctuations were observed in the DSC thermogram, as evident from Figure 5.13 (b). However, the in-situ XRD confirmed no structural transformation of either the major B2-type phase or the minor Cr_5Si_3 type phase in non-equiatomic HEA. The Al matrix was also found to retain its identity until 560 ℃.

Table 5. 6: Physical properties of alloying elements in non-equiatomic HEA.

Parameter	Elements						
	Al	**Si**	**Cr**	**Mn**	**Fe**	**Ni**	**Cu**
Self-diffusion coefficient (m^2/s)	10^{-19}	10^{-62}	10^{-41}	10^{-36}	10^{-31}	10^{-37}	10^{-27}
Thermal conductivity (W/m.K)	238	139	91	8	78	89	397

In the present investigation, the small exothermic fluctuations can be corroborated with the strain relaxation due to MM and dissolution of the minor amount of alloying elements from the non-equiatomic HEA into the Al matrix. Similar observations were made by Basaria et al. [393,419] for Al-Mg-Si-based alloy reinforced with garnet and CNTs. They have shown the minor exothermic fluctuations due to the dissolution of Mg and Si in the Al matrix during the heating of nanocomposite powder in DSC up to 700 ℃ (973 K). The dissolution of alloying elements at higher temperatures can be attributed to the physical parameter like the self-diffusion coefficient, as evident from Table 5.6. The

chances for dissolution of alloying elements with low self-diffusion co-efficient is almost negligible. The elements with higher values of the self-diffusion coefficient and thermal are more prone to dissolve in the Al matrix.

The Al-HEA composite consolidated by pressure-less sintering was found to have appreciable microhardness and yield strength, as illustrated in Table 5.3. However, no signature pertaining to interfacial reaction was evident from the in-situ XRD results or the SEM micrographs of the Al-HEA composite shown in Figure 5.15. However, the interfaces diffused nature was quite prevalent in the Al matrix reinforced with non-equiatomic HEA. The careful examination of the diffused interfaces discerns the presence of a transitional layer (Figure 5.16). Therefore, the enhanced mechanical properties can be ascertained due to the formation of a transitional layer of ~500 nm thickness and HEA particles homogenous distribution in the Al matrix. Apart from the formation of a transition layer between Al and HEA particles, the solid solution strengthening can also be attributed to Al-HEA composites enhanced mechanical properties fabricated by cost-effective pressure-less sintering method. The SEM-EDS mapping shows the presence of elements like Cu, Fe, and Ni in the Al matrix. The intensity of Cu in the Al matrix was very prominent compared to Fe and Ni. This can be attributed to the high self-diffusion coefficient and thermal conductivity of Cu are reported in Table 5.6.

A few researchers and investigators have reported the formation of the transition layer and homogenous distribution of reinforcement responsible for enhanced mechanical properties. In a study, Liu et al. [275] have observed the formation of a transition layer between the Al matrix and AlCoCrFeNi HEA particles. They have discerned the progressive increase in the thickness of the transition layer as a function of SPS temperature varied from 540℃ to 600℃. The increase in the transition layer thickness enhances the

strength of AMCs reinforced with 5 vol% of AlCoCrFeNi HEA particles. They have observed the gradient in the hardness gradually decreases with increasing the transition layer thickness. This may be attributed to the change in the transition layers crystal structure to FCC, due to interfacial reaction between Al matrix and HEA reinforcement having BCC structure. They have discerned the increase in strength may be attributed to the change in stress conditions to iso-strain from iso-stress conditions. In another investigation, Yuan et al. [335] observed the microstructure and properties of 2024 Al alloy reinforced with CoCrFeMnNi HEA known as Cantor alloy. They have discerned the transition layer formation due to the cantor alloys interfacial reaction and 2024 Al alloys. The thickness of transition layer ~6 µm separated into two parts, i.e., the inner diffusion layer and outer diffusion layer with different elemental distribution due to the variation of the diffusion coefficient and modes of the alloying elements Cantor alloy. The formation of gradient transition layers enhances the hardness of AMCs to 135 HV from 80 HV with 7 vol% of HEA reinforcement. The findings reported by Yuan et al. [335] are very close to the present results for Al-10HEA fabricated by pressure-less sintering. The slight deviation in the results can be attributed to the sintering method incorporated.

Similarly, in a recent study, Li et al. [336] have observed the transition layer formation during friction stir processing of $Al_{0.8}$CoCrFeNi HEA reinforced non-age hardenable 5083 Al alloys. The AMCs fabricated by FSP restricts the formation of brittle intermetallic at the interfaces and leads to the formation of Al_3CoCrFeNi HEA as the interfacial layer. This transitional layer having nominal composition very close to non-equiatomic high entropy alloy offers a significant enhancement in the properties due to excellent bonding at the interfaces. Another essential observation was made by Wang et al. [38] and observed the formation of transition layer during the SPS of pure Al matrix and

CuZrNiAlTiW HEA particles having a single BCC phase. The interfacial layer induces the hybridization of AMCs by the formation of B2-NiAl type and WAl_{12} type phases in the transitional layer due to the interfacial reaction. The in-situ formation of B2-NiAl type and WAl_{12} type phases enhances the microhardness of AMCs reinforced with 30 vol% of CuZrNiAlTiW HEA particles and is approximately 10 times more than that of the pure Al. Similarly, due to the formation of core-shell structure in the AMCs reinforced with 10 vol% of HEA demonstrates good comprehensive compressive strength. The excellent mechanical properties of the AMCs can be attributed to the precipitation hardening and dispersion strengthening due to the formation of B2-NiAl type and WAl_{12} type phases and uniform distribution of HEA particles having BCC phase, respectively. Yuan et al. [341] have attempted to fabricate $Al_{0.6}$CoCrFeNi HEA reinforced AMCs by hot pressing followed by heat treatment at 350 ℃, 500 ℃, and 600 ℃ for 24 h. They have observed no distinct transition at the interface of reinforcement and the 5052 Al alloy matrix. However, during heat treatment above 500 ℃, they have discerned the formation of the core-shell structure previously observed by Wang et al. [338]. They have established that the thickness of the interfacial layer was dependent on the heat treatment temperature and the duration of heat treatment [341]. This is indeed due to its dependence on the diffusion coefficient and modes of diffusion.

The high-temperature stability of a major B2-type HEA has led to the synthesis of Al-HEA composite having ~500 nm thick transition layer between the Al matrix and the HEA reinforcement leading to the enhancement of the microhardness and the yield strength of the composite. The interfaces in Al-HEA composite can be engineered for the formation of the transition layer between the Al matrix and HEA particles. This type of interface will inhibit the formation of cracks at the matrix and reinforcement interfaces, as is the case of

MMCs reinforced with ceramic particulates. This strategy will help designing of lightweight AMCs suitable for the automotive sector.

5.8 Conclusions

The mechanical milling of 6082 Al matrix reinforced with the varying volume fraction of non-equiatomic AlSiCrMnFeNiCu HEA up to 50 h of MM and its consolidation by cost-effective pressure-less sintering significantly enhances its grain refinement and microhardness, respectively. The following can be concluded from the present investigation:

1. A non-equiatomic AlSiCrMnFeNiCu high entropy alloy having a primary B2-type phase coexisting with a minor amount of Cr_5Si_3 phase was synthesized by vacuum induction melting.
2. The ratio of $-T\Delta S/\Delta H$ is ~1.05, which is below the threshold limit suggesting the solid solution formation in HEAs as reported in the literature. The VEC and atomic size mismatch factor for this alloy were 5.8 and 5.75, respectively. Although the VEC suggests the formation of BCC phase, the deviation in the phases formed might be attributed to the atomic size mismatch factor variation. Apart from this, the high positive enthalpy of mixing among binary Cr-Cu, Cu-Mn, and Cu-Fe, and high negative enthalpy of mixing among Mn-Si, Cr-Si, Fe-Si, and Ni-Si are also not favorable for the formation of a single-phase high entropy solid solution phase.
3. The non-equiatomic HEA particles in the Al-HEA nanocomposite powder retain their structural characteristics even after 50 h of MM. Increasing the volume fraction of non-equiatomic HEA in Al-HEA nanocomposite powder enhances its nanostructuring with minimum grain size of ~10-12 nm.

4. The Al-HEA nanocomposite powder was found to be thermally stable up to 650 ℃ (923 K) till melting of the Al matrix.
5. The pressureless sintering of Al-HEA composite led to diffused interfaces between the matrix and the reinforcement particles. A transitional layer of ~500 nm thickness was formed at the diffused interfaces in Al-HEA composite.
6. The formation of a transition layer between the non-equiatomic HEA particles and the Al matrix enhances the microhardness and yield strength of Al-30HEA ~1.72 GPa and 486 MPa, respectively.